Chinese Journal of Catalysis 79 (2025) 9–31

available at www.sciencedirect.com

ScienceDirect

journal homepage: www.sciencedirect.com/journal/chinese-journal-of-catalysis

Review

Water interactions in molecular sieve catalysis: Framework evolution and reaction modulation

Linhai He [a,b,1], Caiyi Lou [a,b,1], Lu Sun [a,b], Jing Niu [a], Shutao Xu [a,b,*], Yingxu Wei [a,b], Zhongmin Liu [a,b,*]

[a] *National Engineering Research Center of Lower-Carbon Catalysis Technology, Dalian Institute of Chemical Physics, Chinese Academy of Sciences, Dalian 116023, Liaoning, China*

[b] *University of Chinese Academy of Sciences, Beijing 100049, China*

ARTICLE INFO

Article history:
Received 27 June 2025
Accepted 10 August 2025
Available online 5 December 2025

Keywords:
Water
Molecular sieves
Host-guest interactions
Molecular sieve catalysis
Water-assisted/inhibited catalysis

ABSTRACT

Porous molecular sieve catalysts, including aluminosilicate zeolites and silicoaluminophosphate (SAPO) molecular sieves, have found widespread use in heterogeneous catalysis and are expected to play a key role in advancing carbon neutrality and sustainable development. Given the ubiquitous presence of water during catalyst synthesis, storage, and application, the interactions between water and molecular sieves as well as their consequent effects on frameworks and catalytic reactions have attracted considerable attention. These effects are inherently complex and highly dependent on various factors such as temperature, water phase, and partial pressure. In this review, we provide a comprehensive overview of the current understanding of water-molecular sieve interactions and their roles in catalysis, based on both experimental and theoretical calculation results. Special attention is paid to water-induced reversible and irreversible structural changes in aluminosilicate and SAPO frameworks at the atomic level, underscoring the dynamic and labile nature of these frameworks in water environments. The influence of water on catalytic performance and reaction kinetics in molecular sieve-catalyzed reactions is discussed from two perspectives: (1) its participation in reaction through hydrogen bonding interactions, such as competitive adsorption at active sites, stabilization of ground and transition states, and proton transfer bridge; (2) its role as a direct reactant forming new species via reactions with other guest molecules. Recent advancements in this area provide valuable insights for the rational design and optimization of catalysts for water-involved reactions.

1. Introduction

Molecular sieve catalysts have been widely employed in various crucial chemical processes, exhibiting excellent catalytic performance due to their unique channel structures and tunable acidity properties. These processes include both gas-solid phase catalytic reactions (*e.g.*, fluidized catalytic cracking (FCC) [1], hydrocracking [2], alkylation [3], aromatization [4], and MTH conversion [5–8]) and aqueous-phase biomass conversion and upgrading [9]. Many molecular

* Corresponding author. E-mail: xushutao@dicp.ac.cn (S. Xu), liuzm@dicp.ac.cn (Z. Liu).

[1] Contributed equally to this work.

This work was supported by the National Key R&D Program of China (2022YFE0116000), the National Natural Science Foundation of China (22241801, 22288101, 22022202, 22032005, 21991090, 21991092, 21991093), the Dalian Outstanding Young Scientist Foundation (2021RJ01), and the Liaoning International Joint Laboratory Project (2024JH2/102100005).
https://doi.org/10.1016/S1872-2067(25)64828-5

sieve-catalyzed reactions involve water, which exists as either a vapor or liquid phase, depending on reaction temperature, pressure, and water content. Water can directly participate in these reaction processes as a reactant (via co-feeding), product, or solvent [7,9]. In these processes, the influence of water mainly manifests in two aspects. First, water molecules inevitably interact with Brønsted acid sites (BASs) and T–O–T bonds in molecular sieve frameworks, with the interaction strength strongly influenced by reaction conditions (*e.g.*, temperature, pressure, water content, and water phase) and the intrinsic properties of the molecular sieve catalysts (*e.g.*, framework topology, element composition, and defect density) [10,11]. In the case of weak interaction, the water-induced effects are generally reversible, involving modification of the acid site structure and consequent modulation of their catalytic activity, without framework damage. Conversely, strong interactions can cause irreversible structural changes, resulting in the loss of acid sites and eventual framework degradation. Second, water can directly participate in key elementary steps of catalytic reactions by modulating reactant adsorption, stabilizing intermediates, and altering reaction barriers, thereby significantly influencing aspects including reaction mechanisms, reaction rates, conversion, product selectivity, and catalyst lifetime [12–14]. These water-induced effects can be either positive (enhancing catalytic performance) or negative (causing catalyst deactivation), and this outcome can be precisely modulated by reaction conditions. Thus, comprehending both the interaction mechanisms of water with molecular sieve frameworks and the key roles of water in catalytic reactions has long been central to molecular sieve catalysis research. Advanced characterization techniques—including solid-state nuclear magnetic resonance (ssNMR), Fourier-transform infrared spectroscopy (FT-IR), and X-ray absorption spectroscopy (XAS)—combined with theoretical methods such as density functional theory (DFT) and ab initio molecular dynamics (AIMD) simulations, have enabled systematic insights into the critical scientific issues. These advances provide a foundation for designing molecular sieve catalysts with enhanced hydrothermal stability and optimized performance in water-involved reactions.

To date, several studies have reviewed the water-induced dynamic evolution of the zeolite framework under aqueous or steaming conditions [10,15–17], strategies for enhancing hydrothermal stability [11], water structures on acidic zeolites [18], and the influence of water on heterogeneous catalytic reactions [19,20]. While this topic covers a rather broad range, involving different materials and disparate hydrothermal conditions, a fundamental understanding of water interactions is imperative. This work reviews the water interactions in molecular sieves from fundamental framework change to practical catalytic reaction processes, focusing on the water-induced dynamic evolution of both aluminosilicate and SAPO frameworks. This review is organized as follows: Section 2 presents an overview of water-induced reversible and irreversible structural changes in molecular sieve frameworks as water-molecular sieve interactions intensify, covering water adsorption, reversible hydrolysis of T–O–T bonds, and irreversible hydrolysis of T–O–T bonds. Section 3 discusses the positive and negative roles of water in some molecular sieve-catalyzed reactions from two perspectives: its participation through hydrogen bonding interactions and as a reactant. Section 4 provides a conclusion and outlines future research perspectives associated with water-molecular sieve interactions and the role

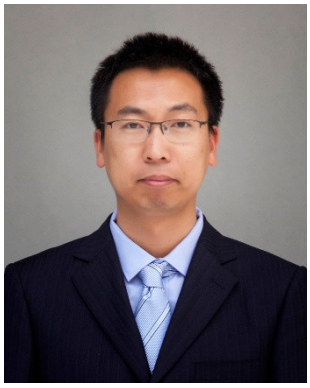

Shutao Xu *(Dalian Institute of Chemical Physics, Chinese Academy of Science) received his B.S. degree from Fudan University (P. R. China) in 2004, and PhD from Dalian Institute of Chemical Physics (DICP), Chinese Academy of Sciences (CAS) in 2011. Then he joined Prof. Zhongmin Liu's team at National Engineering Research Center of Lower-Carbon Catalysis Technology, DICP as a research assistant. He became a professor in 2017. His research interests are the developments various of solid-state Nuclear Magnetic Resonance Spectroscopy (ssNMR) methods, including in-situ/operando techniques, 2D ssNMR spectroscopy, Hyperpolarized (HP)* ^{129}*Xe and Pulse Field Gradient (PFG) NMR, as well as applying these advanced NMR methods to the study of the structure, acidity and reaction mechanism of catalytic materials. He has published more than 100 peer-reviewed papers.*

Zhongmin Liu *(Dalian Institute of Chemical Physics, Chinese Academy of Science) is the Director of Dalian Institute of Chemical Physics (DICP), Chinese Academy of Sciences (CAS) since 2017. He has long been working with the catalysis research, process development, and technology transfer in energy conversion and utilization, and made significant achievements. Prof. Liu led his team to successfully commercialize two of the most representative industrial processes, methanol to olefins (MTO) and methanol to ethanol (MTE), in 2010 and 2017 respectively, which are important advances in coal to chemicals. He has published more than 430 research papers and got 600 authorized patents or more.*

of water in molecular sieve catalysis.

2. Interactions between water and molecular sieves

Water-induced structural changes in molecular sieve frameworks depend on the strength of the host-guest interactions, which can vary from weak to strong, encompassing phenomena such as adsorption, reversible hydrolysis, and irreversible hydrolysis of framework T–O–T bonds (Fig. 1) [10,21]. Adsorption persists throughout the interaction between molecular sieves and water molecules, emphasizing the physical binding of water to adsorption sites without involving chemical hydrolysis of the framework. The latter two interactions involve chemical changes of the framework, but only irreversible hydrolysis leads to structural collapse via the cleavage of T–O–T bonds. When fewer than four water molecules attack the four T–O bonds of a framework tetrahedral T atom (TO_4) and cause irreversible breakage, the T atom remains within the framework as a framework-associated species, a process known as partial irreversible hydrolysis [22]. In contrast, complete cleavage of all four T–O bonds by water molecules leads to the removal of the T atom from the framework, forming extra-framework T species, defining complete irreversible hydrolysis [22]. The loss of a significant number of framework T atoms can generate hierarchical molecular sieves with micropores, mesopores, and/or macropores, or even amorphous materials, thereby affecting both structural integrity and catalytic performance.

2.1. Water adsorption on Brønsted acid sites

The adsorption behavior and structural configurations of water molecules on acidic molecular sieves, including aluminosilicate zeolites and SAPO molecular sieves, have been extensively studied using advanced characterization techniques such as FT-IR [23,24], ssNMR [25–27], and theoretical calculations [23,24,28,29] over the past decades. Water molecules primarily interact with hydrophilic sites on the molecular sieve framework, including Brønsted acid sites (BASs), Lewis acid sites (LASs), and defect sites (*e.g.*, Si–OH species). Given that BASs serve as active sites for numerous hydrocarbon conversion reactions, such as FCC, hydrocarbon cracking, and MTH conversion, this review focuses on the water-BAS interactions and briefly describes the structural configurations of water molecules adsorbed on BAS. Interactions of water molecules with LASs and Si–OH groups are not discussed here but are detailed in a recent review paper by Liu *et al.* [18].

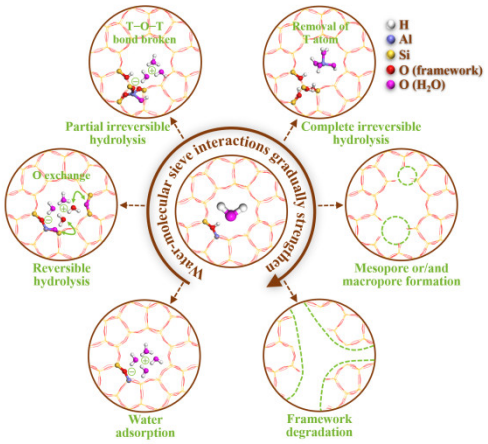

Fig. 1. Schematic illustration of water-induced structural changes in molecular sieve frameworks, with interaction strengths varying from weak to strong, encompassing water adsorption and reversible or irreversible hydrolysis of framework T–O–T bonds.

BAS, *i.e.*, Si(OH)Al, is formed when the negative charge of the framework, arising from AlO_4 units in aluminosilicate zeolites or SiO_4 units in SAPO molecular sieves, is compensated by protons. In the absence of water, the intrinsic BAS exhibits covalent character due to the strong interaction between the proton and the framework oxygen. The H–O bond length of BAS typically ranges from 0.95 to 1.05 Å, influenced by factors such as the topology of molecular sieves and the local chemical environment of the BAS. Upon exposure to water, which acts as a good proton acceptor, water interacts with the BAS through hydrogen bonding. Early studies have debated the adsorption configuration of a single water molecule on BAS, involving the hydrogen-bonded model [30], the protonated model [31], or the coexistence of both models [32]. Currently, it is generally accepted that at low water content (H_2O/BAS = 1), water cannot be protonated but instead forms a hydrogen-bonded neutral complex with BAS, as shown in structure "II" in Fig. 2(a) [24]. The adsorption of a second water molecule (H_2O/BAS = 2) facilitates proton transfer from the framework Si(OH)Al species to water molecules, forming a $H_5O_2^+$ ion-paired complex (*i.e.*, typically "Zundel" cation), as shown in structure "III" in Fig. 2(a), which was supported by IR spectra and theoretical calculations [24,33]. Notably, the proton affinity of the water dimer (806 kJ/mol) is larger than the water monomer (is higher than that of the monomer) (694 kJ/mol), indicating that the protonation of water is more favorable when a second water molecule is present [33]. The DFT-optimized structure of the $H_5O_2^+$ ion-paired complex (structure "III") reveals that this species is relatively unstable, with the proton dynamically rearranging between the framework Si–O–Al bond and dimer [24]. A higher water content (H_2O/BAS > 2) leads to the formation of a larger and fully solvated hydronium ion cluster adjacent to the Al site (structure "IV" and "V" in Fig. 2(a)). As the water loading increases, protonated water clusters enlarge in size, accompanied by an increase in proton affinity [34]. Using DFT and molecular dynamics (MD) simulations, Vener *et al.* [34] identified the water tetramer as the smallest stable water cluster in H-SSZ-13 zeolite, with the water trimer being a short-lived species. These hydronium ion clusters exhibit marked fluxionality, but their overall mobility within the zeolite channels remains limited, as they are primarily confined near BAS rather than diffusing within the zeolite pore [28]. Vjunov *et al.* [24] investigated the redistribution of Bader charge between the proton and water molecules, as well as structural changes during the progressive hydration of BAS on ZSM-5 zeolite, using a combination of physicochemical methods and DFT calculations. They found that proton transfer from the BAS to a water molecule causes the water's positive charge to rise markedly, from 0.18 |e| in

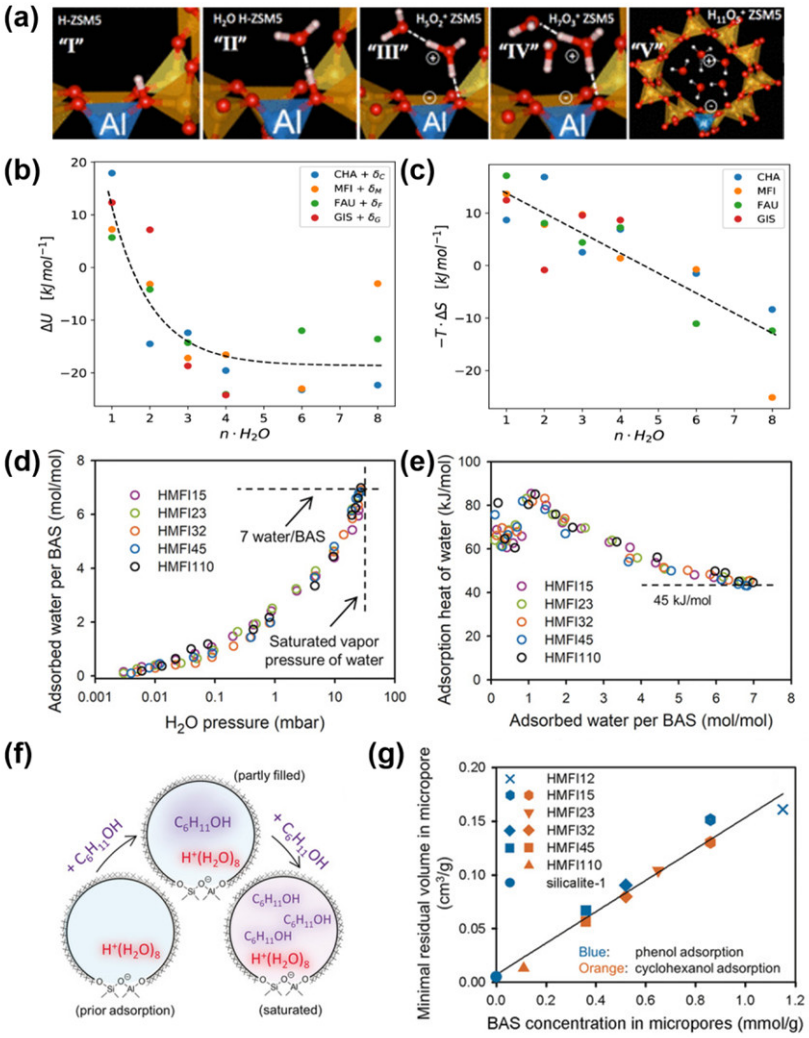

Fig. 2. (a) DFT-optimized structures of Brønsted acid sites in H-MFI zeolite at varying water/BAS ratios. Reprinted with permission from Ref. [24]. Copyright 2017, American Chemical Society. Exponential decay of the enthalpic contributions (b) and linear decay (c) of the entropic contributions to the generation of the hydrated hydronium ion on BAS in various zeolite frameworks (GIS, MFI, CHA, FAU). Reprinted with permission from Ref. [28]. Copyright 2021, Springer Nature. (d) Gas-phase water adsorption isotherm at 298 K for H-MFI zeolites of varying Si/Al ratios. (e) Heat of water adsorption on H-MFI zeolites at varying water/BAS ratios. (f) Schematic of species distribution (hydronium ion clusters and cyclohexanol) within H-MFI micropores before, during partial adsorption, and upon saturation of cyclohexanol. (g) The volume occupied by hydronium ion clusters in H-MFI micropores at saturated adsorption of cyclohexanol and phenol. Reprinted with permission from Ref. [35]. Copyright 2019, John Wiley and Sons.

the neutral complex (H_2O/BAS = 1) to 0.69 |e| for $H_5O_2^+$. As more water molecules are adsorbed on BAS, the hydronium ion's positive charge exhibits only minor increases, reaching 0.70 |e|, 0.72 |e|, and 0.72 |e| for $H_7O_3^+$, $H_9O_4^+$, and $H_{11}O_5^+$, respectively. Correspondingly, the four oxygen atoms bonded to the Al atom carry a more negative charge of 0.10–0.15 |e|. Furthermore, the formation of hydronium ion clusters significantly influences the Al–O bonds in zeolites. Specifically, the Al–O bond linked to the proton is approximately 0.2 Å longer than the other three Al–O bonds. As the proton transfers from the BAS to water molecules, a hydronium ion cluster is formed, accompanied by the four Al–O bonds becoming more equivalent, resulting in similar bond lengths. Grifoni *et al.* [28] evaluated the free energy of stepwise adsorption of water molecules on BAS in various zeolite frameworks (GIS, MFI, CHA, FAU) using a combination of AIMD simulations and enhanced sampling based on the Metadynamics formalisms. At low water content, the standard free energy is predominantly governed by enthalpy (Fig. 2(b)) and is correlated with the acid strength of the BAS and the space around the site. In contrast, as the number of water molecules within the zeolite pores increases, entropy contributions rise nearly linearly (Fig. 2(c)), favoring proton solvation and remaining independent of pore size or shape.

Recently, Eckstein *et al.* [35] measured the composition of hydronium ion clusters within the pores of H-ZSM-5 zeolite with different Si/Al ratios at 298 K using both gas-phase water adsorption and saturated adsorption in cyclohexanol aqueous solution. Gas-phase water adsorption experiments at 298 K revealed that water adsorption uptake per unit weight of zeo-

lite increases as the Si/Al ratio decreases. Notably, after normalizing the adsorption amounts to the BAS concentration, all the adsorption isotherms become identical (Fig. 2(d)), suggesting that water molecules selectively adsorb on BAS. At the saturation vapor pressure of water (31.6 mbar), the number of water molecules per BAS reaches approximately seven. Since the first water molecule adsorbed on BAS interacts only through hydrogen bonding, its adsorption heat is relatively low at 65 ± 5 kJ/mol (Fig. 2(e)). The adsorption of a second water molecule, however, increases the heat to approximately 85 kJ/mol due to proton transfer from BAS to water, forming a protonated water cluster. As more water molecules adsorb, the adsorption heat gradually decreases to about 45 kJ/mol upon reaching seven water molecules per BAS, closely matching the condensation heat of water at 298 K. In aqueous-phase cyclohexanol adsorption experiments, the volume of hydronium ion clusters inaccessible to cyclohexanol was calculated by subtracting the volume of adsorbed cyclohexanol from the micropore volume of the zeolite (Fig. 2(f)). As depicted in Fig. 2(g), this volume is linearly correlated with the concentration of BAS. The space occupied by each hydronium ion cluster was determined to be 239 ± 15 Å^3. Assuming a packing density equivalent to water, each cluster consists of $H^+(H_2O)_8$. The results obtained by both measurement methods are consistent. The same methodology was applied to H-BEA zeolite, revealing the stabilization of a larger $H^+(H_2O)_{10}$ cluster, owing to the lower entropy loss within its larger pores compared to H-ZSM-5 [36]. Additional experimental evidence for hydronium ions in H-ZSM-5 was provided by Wang *et al*. [25], who observed a ^{1}H NMR signal at 9 ppm corresponding to hydronium ions when 2–9 water molecules were adsorbed per BAS. This signal disappeared at elevated temperatures (143 °C), contrasting with the stable hydronium ion clusters observed at room temperature. Notably, the precise structures of water clusters under real reaction conditions of higher temperatures and pressures remain unclear, warranting further exploration to fully understand their dynamic behaviors in these environments.

2.2. Reversible hydrolysis of T–O–T bonds

As water-framework interactions intensify, water molecules can induce the reversible cleavage and reformation of T–O–T bonds, contrasting with the classical perspective of molecular sieves as static and rigid materials. This process is evidenced by $^{17}O/^{18}O$ isotope exchange between the framework oxygen atoms and $H_2{}^{18}O$ or $H_2{}^{17}O$, confirming the water-induced reversible hydrolysis of T–O–T bonds. In the 1980s, Iwamoto *et al*. [37] and Ballmoos *et al*. [38] observed reversible oxygen exchange between water and ZSM-5 or Y zeolite under relatively mild hydrothermal conditions (T = 75 or 90 °C), proposing that framework Si–O–Al and Si–O–Si bonds can be cleaved at measurable rates. Later, by employing $^{17}O/^{18}O$ exchange between water and zeolite framework oxygen atoms at higher temperatures (95–600 °C), along with ^{17}O NMR and ^{18}O IR techniques, a substantial amount of local structural and dynamic information about the zeolite framework oxygen atoms was obtained [39–41]. Recently, using ^{17}O solid-state NMR, Head *et al*. [42] demonstrated that treating SSZ-13 zeolite with neutral liquid $H_2{}^{17}O$ (25 mg zeolite/25 μL $H_2{}^{17}O$) at room temperature (T = 300 K) induces rapid ^{17}O exchange, forming Si–^{17}O–Al and Si–^{17}O–Si species without framework degradation, as shown in Fig. 3(a). This rapid ^{17}O exchange phenomenon was observed in other zeolites, such as MOR [43], FER [43] and MFI [44,45], under similar conditions, providing direct evidence for the reversible hydrolysis of Si–O–Al and Si–O–Si bonds at room temperature and highlighting the lability of the zeolite framework in a water environment. Moreover, a decrease in the ratio of integrated ^{17}O NMR signals for Si–^{17}O–Al and Si–^{17}O–Si with increasing hydration time was observed in CHA, MOR (Figs. 3(b) and (c)), and FER zeolites, indicating a preferential enrichment of Si-O-Al species at shorter hydration times [42,43]. Based on AIMD studies, Head *et al*. [42] also proposed a reversible mechanism for the breakage of Si–O and Al–O bonds in CHA zeolite in neutral liquid water at room temperature. For Si–O bonds, breakage begins with non-dissociative water adsorption on the Si atom, followed by proton transfer via the Grotthuss mechanism, ultimately leading to cleavage of the Si–O bond in the anti-position to the adsorbed water and accompanied by inversion of the SiO_3OH tetrahedron. In the case of Al–O bonds, cleavage involves non-dissociative water adsorption on the Al atom in the anti-position to the BAS, followed by inversion of the $AlO_3{\cdot}H_2O$ tetrahedron. Compared to Si–O bond breakage, Al–O bond breakage occurs with lower free energy barriers. Subsequently, the oxygen exchange mechanism between water and the Al–O and Si–O bonds in acid-form CHA zeolite under steaming conditions was investigated using DFT calculations and AIMD simulations [46]. Com-

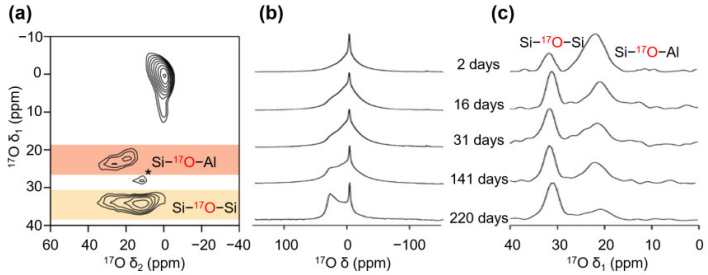

Fig. 3. (a) ^{17}O MQMAS NMR spectra with ^1H decoupling at 14.1 T of SSZ-13/$H_2{}^{17}O$ slurry (25 μL/25 mg) aged 1 h at room temperature. The asterisk (*) denotes the $H_2{}^{17}O$(l) signal. Reprinted with permission from Ref. [42]. Copyright 2019, Springer Nature. ^{17}O MAS (b) and isotropic projections (c) of MQMAS NMR spectra at 14.1 T of H-MOR/$H_2{}^{17}O$ slurry (50 μL/50 mg) recorded after different aging durations. The spectra are normalized. Reprinted with permission from Ref. [43]. Copyright 2019, American Chemical Society.

pared to direct exchange into the pristine framework, oxygen exchange preferentially takes place at the defect sites generated by the first hydrolysis of both Al–O and Si–O bonds, with the exchange of Al–O bond exhibiting a lower energy barrier. The framework healing process involving oxygen exchange is favored over further hydrolysis and also competes with healing processes without exchange. Furthermore, the cooperative effects of two water molecules were examined: adding a second water molecule moderately facilitates oxygen exchange in Al–O bonds but hinders it in Si–O bonds, which was attributed to a combination of defect stabilization, intra-water hydrogen bonding, and steric clashes at the reactive site.

Given that temperature affects the mobility and spatial distribution of water molecules within zeolite channels, the reversible hydrolysis of framework T–O–T bonds at room temperature may exhibit site-specific behavior. Pugh *et al*. [43] found that some Si–O–Si species (observed at low δ_{F1} in ^{17}O MQMAS spectra) in H-MOR zeolite are less susceptible to reversible hydrolysis by $H_2{}^{17}O$(l) at room temperature, compared to oxygen exchange via post-synthesis treatment with $^{17}O_2$(g) at 600 °C. In addition, a comparison of the ^{17}O exchange behaviors of H-MOR and Na-MOR zeolites revealed that the enrichment of ^{17}O occurs more slowly in Na-MOR, suggesting that Na^+ ions inhibit the reversible hydrolysis. Recently, Chen *et al*. [44] and Ji *et al*. [45] treated H-ZSM-5 zeolite with $H_2{}^{17}O$(l) at room temperature, achieving ^{17}O isotope labeling of hydroxyl species in the zeolite framework. Utilizing advanced ^{17}O NMR techniques, including through-bond and through-space polarization transfer experiments, they revealed atomic-scale structural and dynamic insights into various hydroxyl groups, including the bridged hydroxyl groups (BAS), Al–OH groups, and Si–OH groups [45]. Specifically, at room temperature, the proton of BAS (4.1 ppm in ^1H NMR) exhibits low mobility with a jump rate significantly below 100 s^{-1}; Al–OH groups (2.6–2.8 ppm) show a rigid bridging environment similar to BAS; and isolated Si–OH groups (2.0 ppm) undergo fast cone-rotational motion with rates exceeding 10^5 s^{-1}.

Similarly, our work also demonstrated that in SAPO-34, framework T–O–T bonds undergo dynamic and reversible cleavage and reformation under mild hydrothermal conditions (100–300 °C) without framework degradation, as confirmed by the detection of Si–^{17}O–Al and P–^{17}O–Al resonances in 1D and 2D ^{17}O NMR spectra [21]. Based on this reversible evolution of T–O–T bonds induced by water, trimethylphosphine (TMP, 5.5 Å) and pyridine (5.3 Å), both with larger kinetic diameters, were successfully encapsulated into the CHA cavities with a narrow 8-MR window (3.8 × 3.8 Å), *i.e.*, a ship-in-a-bottle strategy, as shown in Fig. 4(a). The adsorption amount of TMP and pyridine is promoted by the presence of water compared with that in the absence of water and further increases progressively with temperature from 100 to 300 °C. Taking pyridine as an example (Fig. 4(b)), at 300 °C, 41.8% of BASs are occupied by pyridine in the presence of water, compared to only 1.3% in its absence. With the assistance of 2D ^1H-^{31}P HETCOR (Heteronuclear Correlation) NMR, ^1H-{^{31}P} REDOR (Rotational Echo Double Resonance) and TMP adsorption energy calculations, four kinds of bridging hydroxyl groups in SAPO-34 were exactly identified for the first time, as shown in Figs. 4(c) and (d), with their acid strength order as B_1 (O_1–H) > B_2 (O_2–H) > B_3 (O_3–H) > B_4 (O_4–H). Additionally, these encapsulated TMP or pyridine

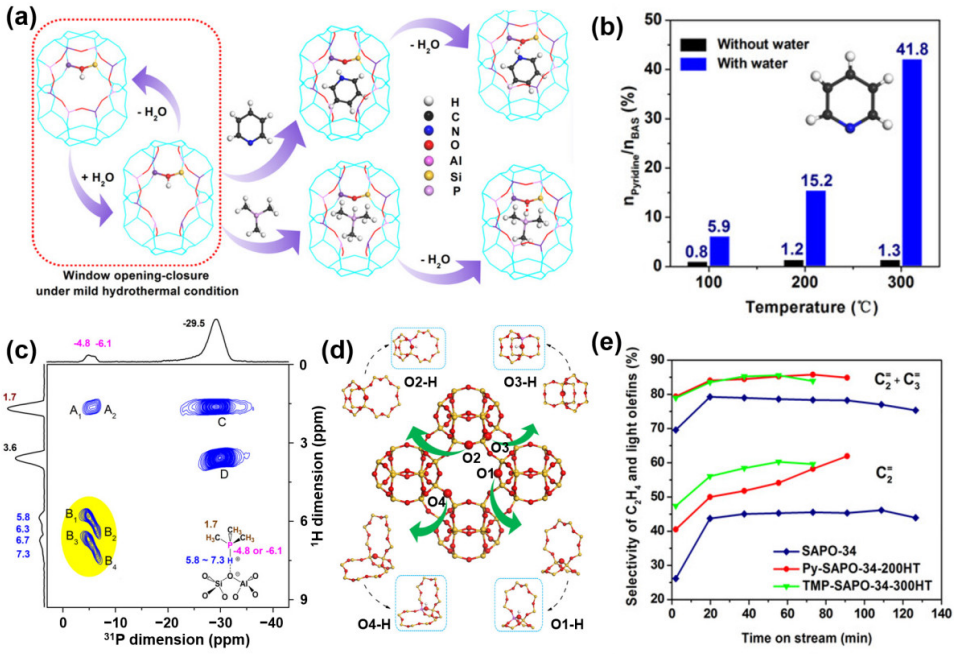

Fig. 4. (a) Encapsulation of TMP and pyridine molecules into CHA cavities via reversible cleavage and reformation of T–O–T bonds under mild hydrothermal conditions. (b) Chemisorbed pyridine content in SAPO-34 with and without water at 100–300 °C. (c) 2D ^1H-^{31}P HETCOR NMR spectrum of TMP-SAPO-34-300HT recorded with a contact time of 3 ms. (d) CHA crystal structure. (e) Selectivity of ethene and light olefins during methanol conversion over fresh SAPO-34, Py-SAPO-34-200HT, and TMP-SAPO-34-300HT, the latter two prepared via hydrothermal encapsulation of pyridine at 200 °C or TMP at 300 °C, respectively. Reprinted with permission from Ref. [21]. Copyright 2020, John Wiley and Sons.

molecules, primarily located on the outer surface of SAPO-34, shift the reaction site to the interior of the catalyst crystal. This configuration significantly enhances the selectivity for light olefins in the methanol-to-olefins (MTO) reaction (Fig. 4(e)) by extending the diffusion path and imposing extra diffusion restriction. Notably, this ship-in-a-bottle strategy, based on the framework's reversible hydrothermal stability, can be used for acidity identification and catalyst modification of molecular sieves with small pore windows.

These studies demonstrate that in water environments, the reversible hydrolysis of framework T–O–T bonds (*i.e.*, rapid and reversible breaking and forming of T–O–T bonds) is a common and significant characteristic, highlighting the framework's dynamic and labile nature rather than its traditional perception as static and rigid. Notably, the ease of reversible hydrolysis at crystallographically inequivalent oxygen sites and its correlation with irreversible hydrolysis stability remain unclear. Additionally, under actual hydrothermal reaction conditions, the influence of water-induced dynamic and reversible bond cleavage and reformation on the adsorption and diffusion behavior of guest molecules (reactants, intermediates and products) cannot be ignored and warrants further investigation.

2.3. Irreversible hydrolysis of T–O–T bonds

Irreversible hydrolysis of framework T–O–T bonds takes place when their interaction with water reaches a critical strength. In catalytic processes involving water, irreversible hydrolysis causes structural changes in the active site (*i.e.*, BAS) and framework degradation, ultimately reducing catalytic activity and lifetime [47]. Therefore, it is crucial to understand both the mechanism by which water molecules attack T–O–T bonds during irreversible cleavage and the dynamic evolution of tetrahedral T atoms. However, this mechanism remains controversial due to the complex structure of water (*i.e.*, single molecules, clusters, and bulk) in the confined environment, which is strongly influenced by conditions such as temperature, partial pressure, and water content [23–25,48,49]. Notably, the hydrothermal instability of frameworks arises from the combined effects of intrinsic factors (topology, heteroatom content and distribution, defect density) and extrinsic factors (water phase, temperature, water partial pressure) [10,50–54]. Hydrothermal stability can be enhanced significantly through strategies such as controlling chemical composition and aluminum distribution (*e.g.*, acid [55] or steaming treatment [56]), applying hydrophobic surface coatings (*e.g.*, organosilanes [26,51], carbon overlayers [57], pure silica coating [58]), reducing external or internal structural defects (*e.g.*, organosilanes [26,51,59], fluoride-mediated synthesis [50] or post-synthesis treatment [60]), and introducing extra-framework phosphorus species [61,62] or metal cations (*e.g.*, Na^+, K^+, Ca^{2+}) [63–65]. A comprehensive review of these advancements is provided by Simancas *et al*. [11]. Herein, we highlight recent advances in understanding the irreversible hydrolysis mechanism of framework T–O–T bonds and identifying key T intermediate species in aluminosilicate zeolites and SAPO molecular sieves.

2.3.1. Aluminosilicate zeolites

In harsh steam conditions, the aluminum centers in aluminosilicate zeolites are susceptible to nucleophilic attack by water molecules, causing the irreversible cleavage of Si–O–Al bonds, a process known as dealumination. This complex process proceeds through the irreversible hydrolysis of all four Al–O bonds. The dynamic evolution of the local structures of tetrahedral aluminum species has garnered increasing attention in catalysis due to their potential catalytic effects, which contributes to the establishment of a well-defined structure-activity relationship. Several theoretical studies have thoroughly investigated the mechanism of dealumination in zeolites, focusing on water molecule adsorption sites, the number of water molecules involved in T–O bond breakage, and the resulting breakage products.

Early studies by Malola *et al*. [66] proposed a dealumination and desilication mechanism of the CHA zeolite, induced by the stepwise hydrolysis of single water molecules, as illustrated in Fig. 5(a). For dealumination, the cleavage of the first three Si–O–Al bonds caused by hydration forms a vicinal disilanol defect, followed by OH group inversion and bond reorientation, resulting in partially bonded $Al(OH)_3$ species and three Si–OH groups. Adsorption of the fourth water molecule forms the final extra-framework $Al(OH)_3{\cdot}(H_2O)$ species. For desilication, the fourth water molecule remains hydrated, eventually forming extra-framework $Si(OH)_4$ species. Although the energy barrier for dealumination (190 kJ/mol) is lower than that for desilication (240 kJ/mol), both processes exhibit relatively high energies. Different from the above dealumination mechanism, Silaghi *et al*. [67,68] proposed a rather universal mechanism for the breakage of the Al–O(H) bond in zeolites such as MOR, FAU, MFI, and CHA, with a lower activation barrier (approximately 76–120 kJ/mol). As shown in Fig. 5(b), the breakage of the Al–O bond begins with the water molecule adsorption on the Al atom in anti-position to the BAS, forming a penta-coordinated or distorted tetrahedral Al species, followed by a 1,2-dissociation of water on adjacent framework oxygen atoms with axial substitution of the silanol. Furthermore, a Brønsted-Evans-Polanyi (BEP) relationship was established to estimate transition states based on the activation energy and water dissociation energy of seven investigated zeolite sites. Recently, Mei and co-workers employed AIMD simulations combined with an enhanced sampling technique to propose a similar dealumination mechanism for H-BEA zeolite, elucidated *via* the S_{N2} mechanism [69]. Each hydrolysis step starts with proton transfer to the $Al–O_{Al}$ bond, followed by an attack of a water molecule at the anti-position of the protonated O_{Al} atom on the Al center, resulting in the simultaneous cleavage of the $Al–O_{Al}$ bond and the formation of an $Al–O_W$ bond.

Additionally, Stanciakova *et al*. [70] studied the cooperative effect of two water molecules in the irreversible breakage of the first Al–O(H) bond, proposing four possible mechanisms that exhibit lower energy barriers relative to the single-water mechanism (Fig. 5(c)). In the first three mechanisms, although the two water molecules exhibit distinct adsorption configura-

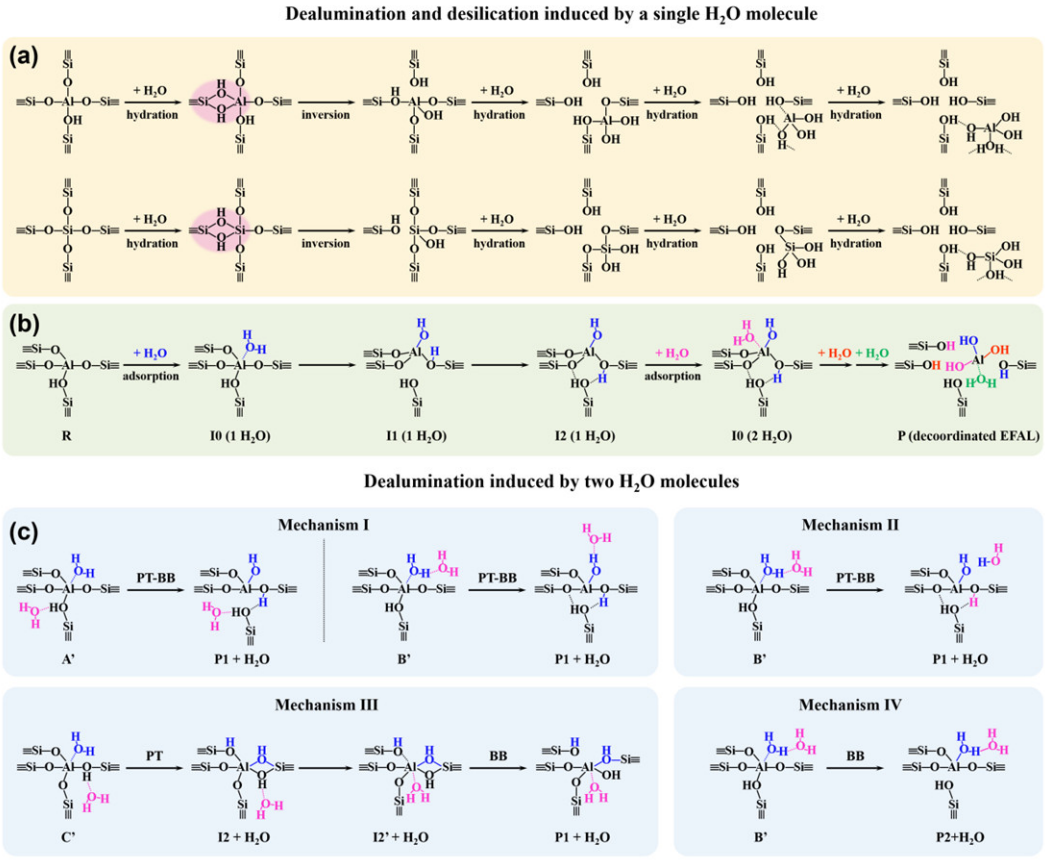

Fig. 5. Schematic illustration of dealumination and desilication processes induced by attack of a single H_2O molecule (a,b) or two H_2O molecules (c). PT and BB in (c) represent proton transfer and Al–O(H) bond breaking, respectively. Reprinted with permission from Ref. [66,68,70]. Copyright 2012, John Wiley and Sons. Copyright 2016, Elsevier. Copyright 2019, American Chemical Society.

tions, the breaking of the Al–O(H) bond is initiated by the adsorption and dissociation of an incoming water molecule. However, the fourth mechanism involves spontaneous Al–O(H) bond breakage, induced by water molecule coordination at the Al atom in the anti-position to the BAS, forming a distorted tetrahedral Al species where the Al atom is bonded to three framework oxygen atoms and one water molecule. Nielsen *et al*. [71], employing DFT-based molecular dynamics (DFT-MD) calculations, also found that cooperation of multiple water molecules lowers the free energy barrier for Al–O bond hydrolysis, in comparison with that for a single water molecule (Fig. 6(a)). Notably, the rate-limiting step in multi-step hydrolysis dealumination differs among zeolites with different frameworks and is influenced by the specific location of the Al atom within the framework [68,69]. Nielsen *et al*. [72] employed a microkinetic model to investigate the dealumination of zeolite H-SSZ-13 by water vapor, finding that the first hydrolysis steps have minimal impact on the dealumination kinetics, while the fourth hydrolysis step serves as the rate-limiting step at temperatures above 700 K.

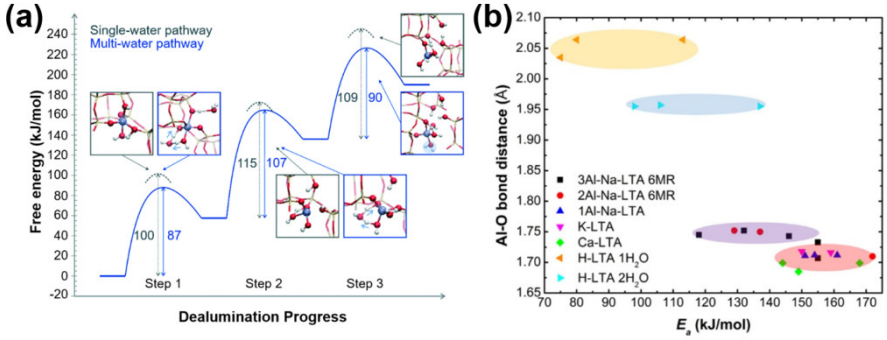

Fig. 6. (a) Free energy diagram of H-SSZ-13 dealumination for the single-water (grey) and multi-water (blue) pathways, calculated using DFT-MD umbrella simulations. Insets show the corresponding transition states. Reprinted with permission from Ref. [71]. Copyright 2019, Royal Society of Chemistry. (b) Correlation between the broken Al–O bonds and activation energies (E_a) in adsorption states. Reprinted with permission from Ref. [63] Copyright 2020, American Chemical Society.

Recently, Sun *et al*. [63] employed plane-wave DFT calculations to investigate and compare the hydrolysis mechanism of the first Al–O bond in LTA zeolites containing different cations (H^+, Na^+, K^+, Ca^{2+}) using DFT calculations. Their results indicated that in H-LTA zeolite, the reaction mechanism involves water dissociation, during which the proton is transferred to neighboring framework oxygen atoms and subsequently rotates to form hydrogen bonds with the BAS oxygen, accompanied by Al–O(H) bond breakage. Cationic LTA follows the same reaction mechanism, but with a second proton transfer, the first Al–O bond does not break simultaneously with H_2O dissociation, resulting in significantly higher energy barriers compared to H-LTA (Fig. 6(b)). Interestingly, the effects of cations (Na^+, K^+, Ca^{2+}) on the hydrolysis of the first Al–O bond are minimal, with comparable reaction barriers observed for all three cations in LTA (Fig. 6(b)). The effect of Al content in Na-LTA was also investigated, with higher Al content found to lower the energy barrier. Furthermore, they found that H_2O at the BAS moderates its activity, leading to a higher activation energy for Al–O(H) bond cleavage when two water molecules are present compared to one (Fig. 6(b)), which contrasts with previous studies [70,71]. These theoretical calculations suggest that, regardless of the adsorption site (BAS or framework Al atom in anti-position to the BAS) or the number of water molecules involved (one or two), water-induced zeolite framework dealumination follows a stepwise hydrolysis process, sequentially forming framework-associated Al species with terminal Al–OH groups and extra-framework $Al(OH)_3{\cdot}H_2O$ species.

The experimental identification of key Al intermediate species during the dealumination process is crucial for rationalizing the mechanism of irreversible hydrolysis. Recently, partially coordinated tetrahedral Al species (denoted Al(IV)-2), previously predicted by theoretical calculations as intermediates formed via partial irreversible hydrolysis of framework Al, were experimentally observed in dry steam-treated H-ZSM-5 zeolite using 2D $^{27}Al\{^1H\}$ correlation NMR techniques at 35.2 T by Chen *et al*. [73,74]. In the $^{27}Al\{^1H\}$ D-HMQC spectra of dehydrated H-ZSM-5 (Fig. 7(a)), the signal region labeled ii correspond to the bridged hydroxyl groups of Al(IV)-1 species, while those labeled i, iii, and iv are attributed to Al(IV)-2 species and its associated hydroxyl groups (Fig. 7(b)). Relative to Al(IV)-1 species, Al(IV)-2 species exhibits a higher chemical shift and smaller quadrupolar interaction product (P_q) in the dehydrated state, whereas in the hydrated state it shows a larger P_q and an apparent lower chemical shift in the hydrated state. Remarkably, Al(IV)-2 species can be completely removed by mild washing with ammonium hexafluorosilicate (AHFS) (Figs. 7(c) and (d)). Further characterization with TMP as a probe molecule revealed that Al(IV)-2 species forms an Al–OH···$P(CH_3)_3$ complex with a unique ^{31}P NMR resonance at –58 ppm [75]. Additionally, Al(IV)-1/Al(IV)-2 pairs, *i.e.*, "BAS and Al(IV)-2", were found to be in closer spatial proximity than either "BAS and LAS" or framework Al(IV)-1/Al(IV)-1 pairs [44,75]. H-ZSM-5 zeolite catalysts containing Al(IV)-2 species exhibit higher reactivity in reactions such as benzene hydride transfer and n-hexane cracking compared to zeolite with only Al(IV)-1 species [74]. He *et al*. [53] demonstrated that Al(IV)-1 species in H-ZSM-5 zeolite sequentially transform into Al(IV)-2 species and eventually into extra-framework aluminum (EFAL) species via partial and complete hydrolysis, respectively, by precisely controlling steam temperature and treatment time. Al(IV)-2 species were also detected in other zeolites, such as H-SSZ-13 [49] and H-MOR [76], during steam-induced dealumination.

More recently, Zheng *et al*. [77] demonstrated the genera-

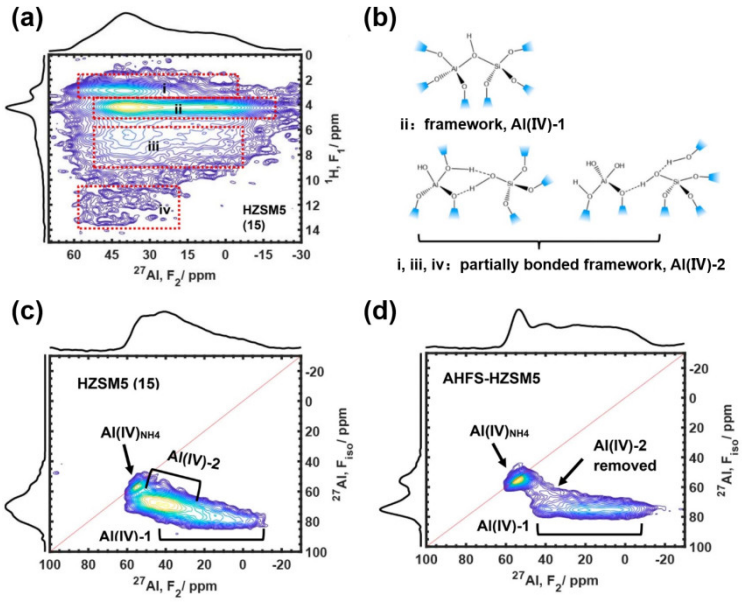

Fig. 7. (a) $^{27}Al\{^1H\}$ D-HMQC spectra of dehydrated H-ZSM-5 (Si/Al = 15) acquired at 19.6 T. The signal regions labeled ii arise from Al(IV)-1 species, while those labeled i, iii, and iv arise from Al(IV)-2 species and its associated hydroxyl groups. (b) Schematic diagram of the structures of Al(IV)-1 and Al(IV)-2 species. (c) ^{27}Al MQMAS spectra of dehydrated H-ZSM-5 (Si/Al = 15) recorded at 19.6 T before AHFS washing and (d) after AHFS washing. Reprinted with permission from Ref. [73]. Copyright 2021, American Chemical Society.

tion of Brønsted acidic penta-coordinated Al species (Al(V)-BAS) during the dealumination of H-Y and H-SSZ-13 zeolites, as revealed by advanced proton-detected 2D J coupling mediated (through-bond), MQMAS-based $^{1}H\{^{27}Al\}$ heteronuclear correlation experiments and DFT calculations. This species is associated with two bridging hydroxyl groups (δ_{1H} = 3.9 ppm) and one Al–OH group (δ_{1H} = 2.7 ppm), as depicted in Fig. 8(a). Pyridine-d_5 adsorption experiments (Fig. 8(b)) further revealed that, compared to traditional BAS (Al(IV)-1), the Al(V)-BAS exhibits stronger Brønsted acidity. Based on Al(V)-BAS, they proposed a new dealumination mechanism in which a water molecule adsorbs onto the Al atom in the anti-position to the BAS (Fig. 8(c)), followed by its direct dissociation on framework Al(IV) sites, without breaking the Al–O–Si bonds. Although the energy barrier for forming Al(V)-BAS (45.13 kcal/mol) is higher than that for partially coordinated tetrahedral Al species (Al(IV)-2) with one BAS and Al–OH group (35.32 kcal/mol), the formation of Al(V)-BAS remains achievable, particularly at elevated temperatures.

The initial extra-framework $Al(OH)_3{\cdot}(H_2O)$ species formed by dealumination can further transform into new forms, including cations such as $Al(OH)_2^+$, $Al(OH)^{2+}$, AlO^+, Al^{3+} or neutral forms like $Al(OH)_3$, AlO(OH), Al_2O_3 or their clusters (dimers, trimers), which act as LASs essential for zeolite catalytic properties [22,78,79]. These EFAL species exhibit complex host-guest interactions with the zeolite frameworks. Early work by Yu *et al*. [80,81] using ^{27}Al and ^{1}H double-quantum (DQ) NMR experiments on dealuminated H-MOR, H-ZSM-5, and H-Y zeolites revealed that six-coordinated and five-coordinated EFAL species, along with four-coordinated framework aluminum (Al(IV)-1), are in close spatial proximity. The resulting Brønsted/Lewis acid synergistic effect between Al(IV)-1 and EFAL species remarkably enhances the acid strength of BASs, thereby affecting catalytic activity [82-84]. Recently, Pham *et al*. [82] reported that the presence of water facilitates the migration of EFAL species generated by hydrolysis to positions near the BAS, forming synergistic sites that enhance the catalytic activity for *n*-hexane cracking. Very recently, Wang *et al*. [84] revealed that the dissociative adsorption of water on "NMR-invisible" aluminum species (tricoordinated framework Al and cationic EFAL) in ultrastable Y zeolite under ambient conditions transforms them into "NMR-visible" Al species, as evidenced by solid-state NMR spectroscopy and theoretical calculations. This transformation generates new BASs on four-, five-, and six-coordinated framework Al species, leading to a substantial (> 60%) increase in the BAS concentration. These newly formed BAS, in proximity to LAS, generate Brønsted/Lewis acid synergistic sites, enhancing Brønsted acidity and significantly improving catalytic performance in the conversion of diethyl ether to ethene under moderate water content conditions.

Unlike in steam environment, the zeolite framework exhibits its distinct thermal susceptibilities in hot liquid water (HLW), with Si–O–Si bonds showing lower hydrothermal stability than Si–O–Al bonds [52,85]. Even at temperatures as low as 200 °C in HLW, rapid structural collapse and a dramatic decrease in crystallinity were observed within a few hours, primarily as a result of the irreversible breakage of Si–O bonds. Ravenelle *et al*. [86] proposed that the irreversible breakage of Si–O–Si bonds is catalyzed by hydroxyl ions (OH^-) and that of Si–O–Al bonds by protons (H^+). The significant increase in equilibrium concentrations of ionic species (H^+ and OH^-) in HLW, resulting

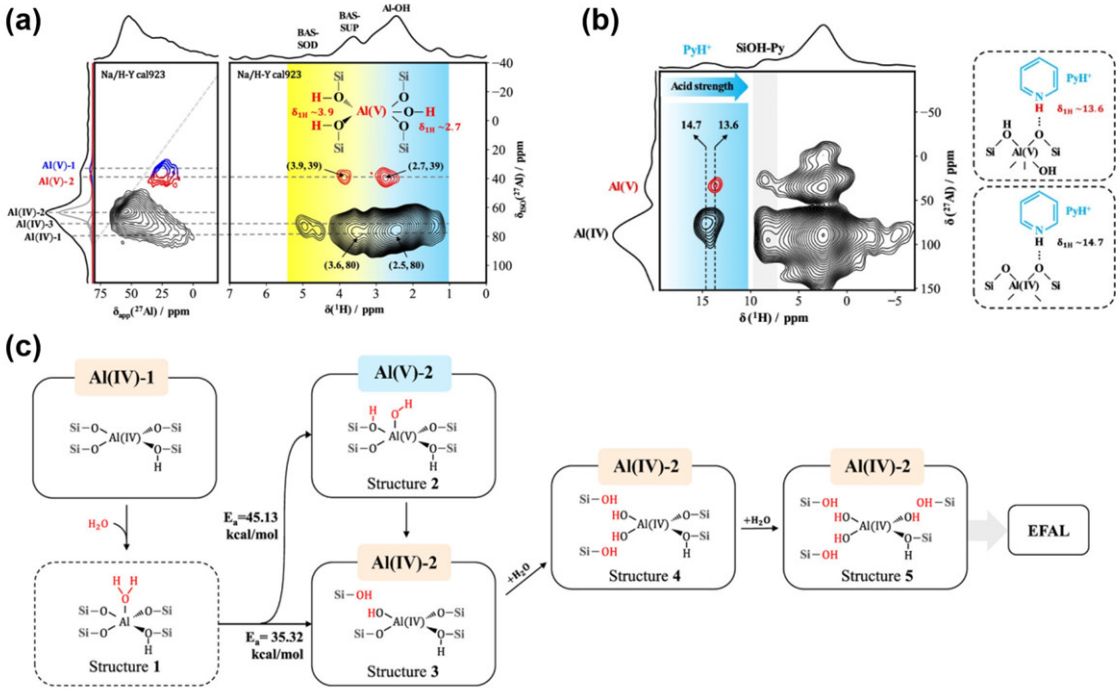

Fig. 8. (a) ^{27}Al MQMAS (left) and $^{1}H\{^{27}Al\}$ MQ-D-RINEPT (right) spectra of dehydrated Na/H-Y cal923 zeolite (calcined at 923 K in air). (b) $^{1}H\{^{27}Al\}$ MQ-D-RINEPT spectra of dehydrated H-Y cal923 (calcined at 923 K in air) after pyridine-d_5 adsorption. All spectra were recorded at 18.8 T. (c) Proposed zeolite dealumination mechanism. Reprinted with permission from Ref. [77]. Copyright 2024, American Chemical Society.

from the rise in auto-ionization constant of water from 1 × 10^{-14} at 25 °C to 1 × 10^{-10} at 300 °C, facilitates the cleavage of both Si–O–Si and Si–O–Al bonds [87]. Notably, although extensive studies have shown that zeolite instability in HLW environments is largely governed by the density of defect sites [50,51,59], the specific reaction mechanism for Si–O bond cleavage initiated at these defect sites remains unexplored. Although the rapid collapse of zeolites in HLW is primarily attributed to Si–O bond breakage, increasing attention has focused on the structural evolution of framework tetrahedral Al (Al(IV)-1), which provide active sites in aqueous catalytic reactions such as biomass conversion and upgrading. Vjunov *et al*. [88] explored the behavior of Al(IV)-1 species in H-BEA zeolites under HLW conditions using Al extended X-ray absorption fine structure (EXAFS) analysis and ^{27}Al NMR spectroscopy. Their findings revealed that for HZBEA zeolite (Si/Al = 25), framework collapse at 160 °C is due to irreversible hydrolysis of Si–O–Si bonds, while the local structure of framework Al atoms, including Al–O–Si angles and bond distances, remains mostly intact. At 300 °C, however, the irreversible hydrolysis of Si–O–Al bonds (dealumination) also occurs, as evidenced by nearly all Al atoms being present in octahedral coordination at 6.3 ppm in ^{27}Al NMR spectra. Similar behaviors of Si–O–Si and Si–O–Al bonds were also observed in ZSM-5 [52] and ZSM-22 [85] zeolites. Recently, He *et al*. [52] reported that Al(IV)-1 species in HLW evolved similarly to its behavior in steam, forming partially coordinated tetrahedral Al species (Al(IV)-2) and EFAL species sequentially.

2.3.2. Silicoaluminophosphate (SAPO) molecular sieves

Compared to aluminosilicate zeolites, SAPO molecular sieves generally exhibit inferior structural stability in humid environments, despite their exceptional hydrothermal stability at relatively high temperatures [54,89]. Extensive early studies have revealed that the framework degradation of SAPO molecular sieves involves irreversible hydrolytic cleavage of P–O–Al and Si–O–Al bonds. The following evidence supports P–O–Al bond hydrolysis. Parlitz *et al*. [90] investigated the structural damage of AlPO-17, SAPO-5, SAPO-17, and SAPO-44 after treatment with 0.2 N ammonium acetate solution under nearly neutral (pH = 6.4) conditions, showing that all frameworks were attacked by water within the temperature range of 323–473 K. The observed structural collapse originated specifically from P–O–Al bond cleavage, not from Si–O–Al bond sites. Zubowa *et al*. [91] proposed that the hydration of SAPO-31 involves both the interaction of tetrahedral framework aluminum with adsorbed water molecules and the hydrolysis of some Al–O–P bonds, as evidenced by the strong enhancement of a new signal at –23.4 ppm (assigned to P–OH species) in ^{31}P CP MASNMR spectra. Buchholz *et al*. [89] systematically compared the framework degradation of SAPO-34 and SAPO-37 during successive steps of hydration (vapor) and dehydration using *in-situ* ^{1}H and ^{27}Al continuous flow (CF) MAS NMR spectroscopy. They proposed that the framework hydrolysis was initiated by the cleavage of P–O–Al bonds, whereas Si–O–Al bonds remained intact, as no Si–OH groups were detected in ^{1}H MAS NMR spectra during the hydration process at 298 K and dehydration at 298–413 K. On the time scale of the *in-situ* NMR experiments, P–O–Al bond hydration is reversible in SAPO-34 but proceeds irreversibly in SAPO-37. In addition, the superior stability of SAPOs at higher temperatures was explained as follows: water molecules preferentially hydrated Brønsted acid sites (bridging OH), rather than coordinated with aluminum atoms under high-temperature conditions ($T \geq 353$ K for SAPO-37) which caused the hydrolysis of P–O–Al bonds and consequent structural degradation. Irreversible hydrolysis of Si–O–Al bonds (desilication mechanism) was also demonstrated, as indicated by the appearance of new and distinct types of silicon species following water treatment. For example, Lourenço *et al*. [92] found that new silicon environments, ranging from –95 to –120 ppm, were detected by ^{29}Si NMR after SAPO-40 rehydration at room temperature, which remained after dehydration at 200 °C. Similar changes in the ^{29}Si NMR spectra were reported in SAPO-34 by Vomscheid *et al*. [93] and Arstad *et al*. [94], who observed a modified spectrum characterized by the emergence of Q1, Q2 or extra-framework silicon after exposure to moisture (ranging from hours to months) or thermal steaming. Briend *et al*. [95] reported that organic template choice influenced silicon distribution and further framework stability. Bauer *et al*. [96] found that the low-silicon SAPO-34 sample underwent reversible structural changes, whereas the high-silicon SAPO-34 experienced fast irreversible structural degradation.

Recently, based on the proposed dealumination and desilication mechanisms of SSZ-13 zeolite [66], Fjermestad *et al*. [97] simulated an analogous desilication process (forming a vicinal disilanol intermediate) in SAPO-34, which shares the same chabazite topology as SSZ-13, and compared it to the dealumination process in SSZ-13 using DFT. They found that only the structures associated with the hydrolysis of the first T–O–T bond was qualitatively similar in both zeolites, while the mechanisms of the subsequent three hydrolysis steps diverged (Fig. 9(a)). In the corresponding intermediates, a Brønsted proton was bonded to an oxygen atom bridging the Al and Si atoms in SSZ-13, whereas in SAPO-34, the same proton preferred to be part of an aqua ligand coordinated to an Al atom in the vicinity of the Si heteroatom. Notably, the transition state energy of the first hydrolysis step was 195 kJ/mol for SSZ-13 and 119 kJ/mol for SAPO-34, which can be attributed to the strong Si–O bond and the weaker Al–O bond being broken. Later, they proposed two new desilication mechanisms in SAPO-34 with lower transition state energies, both involving water molecules strongly adsorbed on aluminum atoms neighboring the Si atom [98], similar to the dealumination mechanism reported by Silaghi *et al*. [67]. In one mechanism, only a single water molecule adsorbed on an Al atom neighboring the Si atom, decreasing the transition state energy from 119 to 94 kJ/mol (Fig. 9(b)). This reduction resulted from water adsorption at the Lewis acidic Al site, which enhanced the acidity of the water molecule's protons, facilitating proton transfer. In another mechanism, a second water molecule absorbed (adsorbed) on BAS (Fig. 9(c)), acting as a catalyst, further reduced the transition state energy of the first T–O–T bond hydrolysis to just 8 kJ/mol. The authors emphasized that dis-

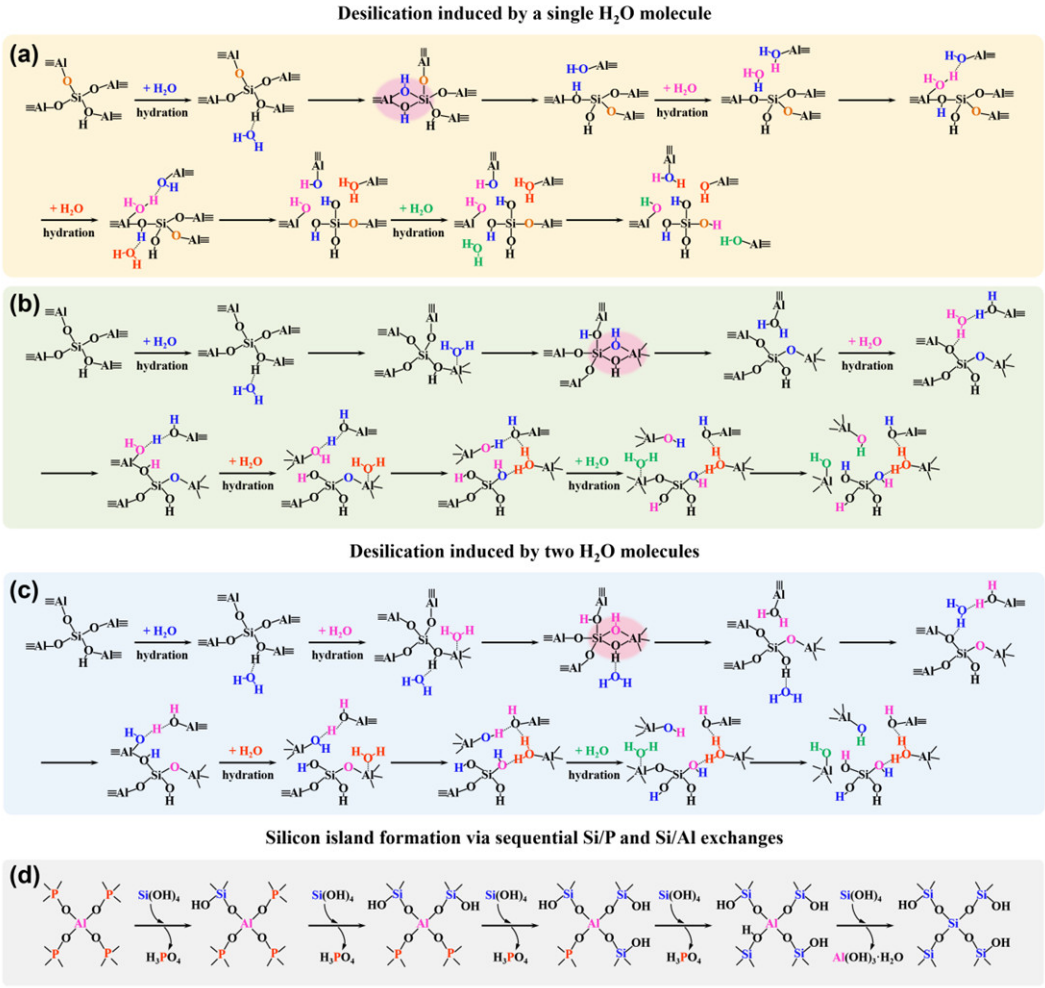

Fig. 9. Schematic illustration of desilication mechanisms induced by attack of a single H_2O molecule (a,b) or two H_2O molecules (c), and silicon island formation (d) *via* sequential Si/P and Si/Al exchanges within the SAPO structure. Reprinted with permission from Ref. [97–99]. Copyright 2013, American Chemical Society. Copyright 2015, American Chemical Society. Copyright 2015, American Chemical Society.

persion and free energy corrections were necessary for the processes associated with water adsorption, although the overall energy profile remained qualitatively unchanged. Additionally, a dephosphoration mechanism initiated by the adsorption of a water molecule on an Al atom in SAPO-34 was also proposed [99]. Compared to desilication (145 kJ/mol), dephosphoration exhibited a larger free energy span (189 kJ/mol) at T = 298 K and P_{H2O} = 0.02 atm. Furthermore, they investigated the formation mechanism of Si island in SAPO-34, which led to irreversible deactivation in catalysis, involving the mobilization and exchange of framework Si and P atoms caused by the irreversible hydrolysis of T–O–T bonds (Fig. 9(d)) [99]. Specifically, the process begins with the removal of a Si atom from the framework, generating extra-framework $Si(OH)_4$ species. Simultaneously, an available extra-framework H_3PO_4 species, derived from P atoms in defects or at the external surface of the crystal, inserts into the hydrogarnet defect formed by desilication. The generated $Si(OH)_4$ species then replaces a framework P atom, while "kicking out" the P atom as an extra-framework H_3PO_4 species for subsequent Si/P exchange. This continued Si/P exchange transforms $Al(OP)_4$ units into $Al(OSi)_4$ units, followed by Si/Al exchange that gives rise to Si islands, represented as $Si(OSi)_4$ units, within the SAPO framework.

Although understanding the irreversible hydrolysis of SAPO molecular sieves is of considerable scientific and practical importance, their degradation mechanisms remain a topic of debate. Special attention should be paid to distinguishing between general degradation mechanisms applicable to all SAPOs and specific mechanisms associated with particular SAPO types. Compared to the extensive studies on aluminum species in aluminosilicate zeolites, defect-related species in SAPOs lack detailed and precise structural characterization. Expanding the atom-scale characterization of their local framework structure is imperative and should be a focus of future research. For example, Al(VI) species, converted from pristine tetrahedrally coordinated aluminum species (Al(IV)), are consistently observed in SAPO materials during hydration via ^{27}Al MAS NMR. In aluminosilicate zeolites, the formation of these species typically indicates framework dealumination or partial hydrolysis. Therefore, understanding the nature of these species contributes to a deeper comprehension of SAPO stability. However, the

precise structural identity of these Al(VI) species remains ambiguous, due to the underlying heterogeneity of Al(VI), framework lability (involving rapid and dynamic transformations), challenges in distinguishing hydroxyl groups from adsorbed water, and the quadrupolar nature of ^{27}Al nucleus.

2.4. Effects of water on molecular sieve frameworks during reaction

The structural changes of molecular sieve catalysts during reactions are closely linked to their activity and lifetime, thus garnering considerable attention. Unlike simple water-molecular sieve systems, water-framework interactions during reactions are significantly influenced by other guest molecules (*e.g.*, reactants, intermediates, and products). Recently, Yang *et al.* [100] investigated water-induced structural changes of fresh SAPO-34 catalysts after methanol-to-olefins MTO conversion at 623 K for varying time on stream (TOS) (0–3 h), using 1D ^{31}P and ^{27}Al MAS NMR along with 2D ^{31}P-^{27}Al HETCOR MAS NMR. Their study revealed that, for spent SAPO-34 catalysts after short TOS, P–O–Al bonds are irreversibly hydrolyzed, whereas Si–O–Al bonds remain unbroken, which is evidenced by the P(V) signal at –15.4 ppm in the ^{31}P MAS NMR spectra and the absence of Si–OH signals at 1.8 ppm in the ^{1}H MAS NMR spectra. As MTO conversion progresses, organic deposits increasingly accumulate within the CHA cages, partially covering BAS and even some P–O–Al bonds, thus effectively protecting the framework from irreversible hydrolysis. More recently, Wang *et al.* [101] identified preferential steam-induced dealumination sites in H-ZSM-5 zeolite during recursive MTH reaction–regeneration cycles using ^{27}Al and ^{1}H-^{1}H DQ-SQ MAS NMR and diffuse-reflectance UV-vis spectroscopies. They found that tetrahedral Al atoms situated in channels exhibited a higher dealumination propensity than those facing intersections, with dealumination occurring randomly at both isolated and proximate Al sites.

3. Roles of water in molecular sieve catalysis

Water, commonly serving as a reactant, product, or reaction medium, plays complex and diverse roles in catalytic reactions. Through adsorption at active sites on molecular sieve catalysts, direct participation in reaction pathways, and regulation of guest molecule diffusion behavior, water significantly influences active site utilization, reaction rates, reaction pathways, conversion efficiency, product selectivity, coke formation mechanisms and distribution, as well as catalyst stability and lifetime. These water-induced effects can be either positive or negative, depending closely on reaction temperature, pressure, and water content. In this section, we discuss the essential roles water plays in various catalytic reactions and its impact on catalytic performance from two perspectives: its participation in reactions through hydrogen bonding interactions and as a reactant.

3.1. Participation in reaction via hydrogen bonding

3.1.1. Competitive adsorption on active sites

Competitive adsorption between water molecules and reactants, intermediates, or products at active sites is a widely recognized and critical mechanism in gas-solid heterogeneous catalytic reactions. Through hydrogen bonding, water molecules interact with the acidic protons of the BAS, thereby hindering the adsorption and activation of reactant molecules on these active sites. Taking the MTO reaction as an example, this process produces light olefins (ethene and propene) from non-oil feedstocks such as coal, natural gas, and biomass. Competitive adsorption of water against methanol and the initial product (*i.e.*, propene) at BAS on SAPO-34 reduces the likelihood of activating methanol to form methoxy species (SMS) and propene to form cyclic hydrocarbon pool species (HCPs) [102]. This effect becomes more pronounced with increasing water loading. MD simulations of SAPO-34 containing only methanol ($(5{:}0)_{mw,sim}$) (Fig. 10(a)) and a methanol-water mixture ($(1{:}4)_{mw,sim}$) (Fig. 10(b)) revealed that, in the presence of water, methanol cannot access a proton during a significant time in the simulation, preventing its activation for further reactions. Specifically, the free energy barrier for methoxide formation increases from 123 ± 2 kJ/mol for $(5{:}0)_{mw,sim}$ to 147 ± 5 kJ/mol for $(1{:}4)_{mw,sim}$. These water-induced effects collectively prolong the MTO induction period, with longer durations observed at higher co-feeding water content (Fig. 10(c)), as confirmed by UV-vis microspectroscopy experiments. Slower HCPs formation alleviates diffusion limitations, allowing methanol and propene to access the crystal interior more effectively, thereby enhancing the utilization efficiency of inner BASs and causing a more uniform distribution of intermediates and coke deposits (Figs. 10(d)–(f)). These water-induced effects were also observed in a recent study by Zhang *et al*. [103] during the high-pressure MTO reaction catalyzed by SAPO-34. Notably, in the MTO process, competitive adsorption between water and methanol, oxygenates, or HCPs reduces their accessibility to BASs, thereby attenuating many steps in the reaction network and ultimately decreasing coke formation rates while prolonging catalyst lifetime [103–111]. Therefore, co-feeding water has been established as an effective strategy for depressing the formation of coke species during the MTO process. In the work of Baranowski *et al*. [112], the deleterious effect of water on the kinetics of oxymethylene dimethyl ether (OME) synthesis from dimethoxymethane (OME_1) and trioxane (TRI) over H-beta zeolite was revealed through kinetic analysis and *in-situ* infrared spectroscopy. At 30 °C and ambient pressure, water significantly inhibited the conversion of TRI, with the inhibitory effect increasing at higher water concentrations. Arrhenius analysis further showed that increasing the water concentration in OME_1 from 0.03 wt% to 0.44 wt% raised the apparent activation energy from 96.1 to 100.7 kJ/mol and decreased the frequency factor by over an order of magnitude, from 1×10^{14} to 2×10^{12}, highlighting the significant influence of water on the reaction kinetics. Since the surface affinity follows the order $OME_1 > H_2O > TRI$, as confirmed by ATR-IR spectroscopy and DFT simulations, this inhibition was attributed to competition between water and TRI for BAS. Consequently, the presence of water shifted the chain growth mechanism from direct TRI

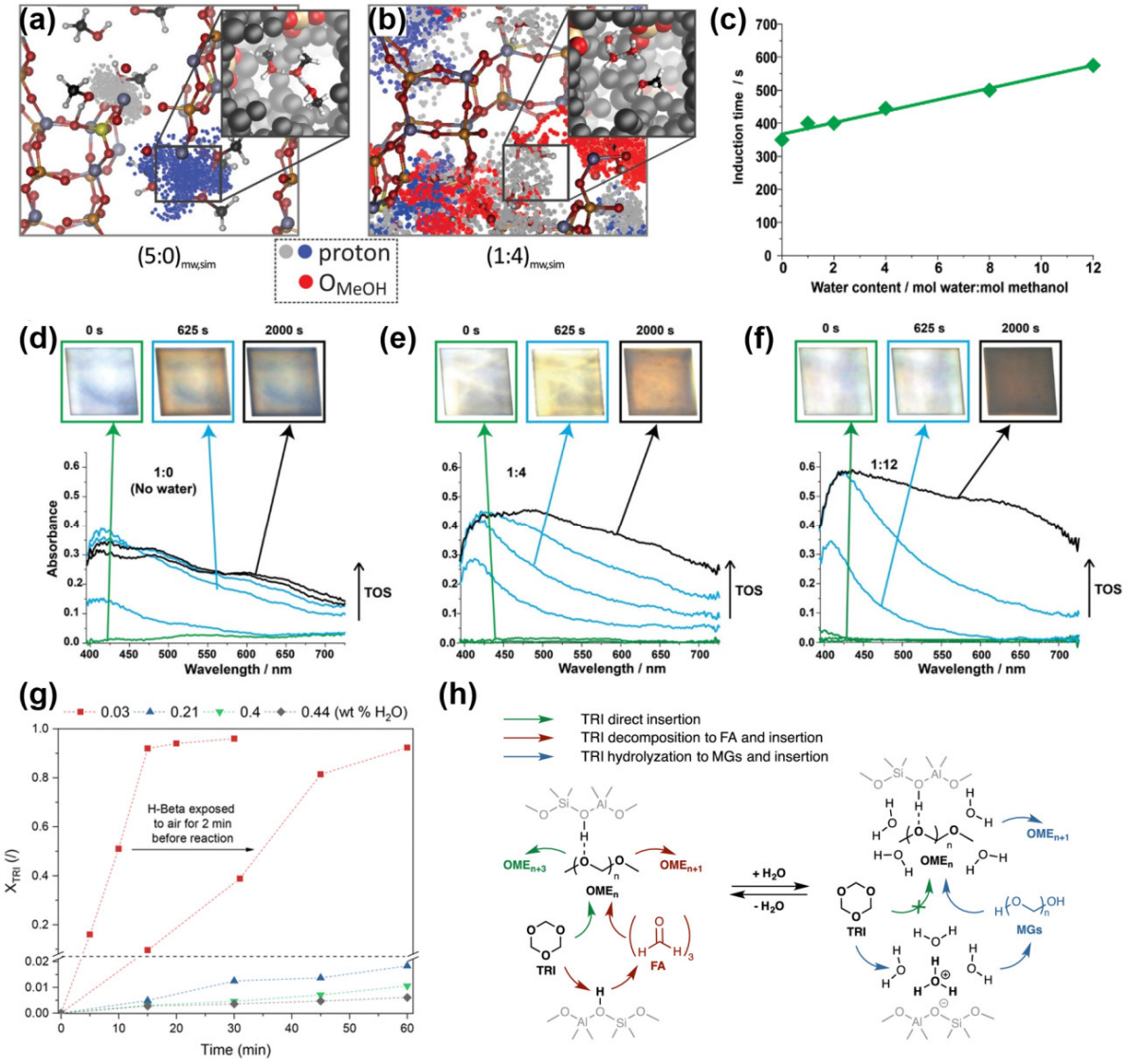

Fig. 10. (a,b) SAPO-34 loaded with methanol-water mixture (5:0 and 1:4 per BAS) at 330 °C and around ambient pressure. $(x{:}y)_{mw,sim}$ indicates *x* MeOH and *y* H_2O molecules per BAS in the simulation. (c) Induction times of single H-SAPO-34 crystals was monitored via *in-situ* UV-vis microspectroscopy as a function of water content. Optical images and UV-vis spectra of single SAPO-34 crystals during MTO with methanol-water ratios of 1:0 (d), 1:4 (e), and 1:12 (f); showing progression from induction period (green) to aromatic formation (blue) and deactivation (black). Reprinted with permission from Ref. [102]. Copyright 2016, American Chemical Society. (g) Conversion of TRI (X_{TRI}) during OME synthesis over H-beta zeolite at varying water contents in OME_1 (T = 30 °C, 0.5 wt% catalyst, OME_1:TRI = 3.3). (h) Schematic illustration of the proposed mechanism of water inhibition during OME synthesis over H-Beta zeolite. Reprinted with permission from Ref. [112]. Copyright 2020, American Chemical Society.

insertion or TRI dissociation with subsequent incorporation of formaldehyde units to TRI hydrolysis, forming methylene glycol units that were then inserted into the OME chain. Recently, Kung *et al*. [113] reported that water loading modulates the structure of water-methanol complexes at BAS in H-ZSM-5, thereby influencing the initial rate of dimethyl ether (DME) formation. For samples containing ~1.5 equiv. methanol of or less, the activity increased with increasing water loading, as the inactive hydrogen-bonded complex ($CH_3OH{\cdot}HZ$) was transformed into the more-reactive solvated proton complex ($(H_2O{\cdot}CH_3OH_2)^+{\cdot}Z^-$). At around 1.6–1.9 equiv. of methanol, water addition had little effect. At higher methanol loadings, methanol-methanol complex ($(CH_3OH{\cdot}CH_3OH_2)^+{\cdot}Z^-$) became the dominant species, and its concentration and reactivity with methanol were reduced due to competition from water, leading to a gradual decline in dehydration activity with increasing water loading.

Moreover, the desorption of reactant or product molecules is also affected by the competitive adsorption of water, thereby influencing catalytic performance [114,115]. Brosius *et al*. [114] reported that water's competitive adsorption facilitates the desorption of primary n-C_{16} cracking products, inhibits secondary cracking, and achieves 80% selectivity for linear alkanes and 80% conversion in the hydrocracking of

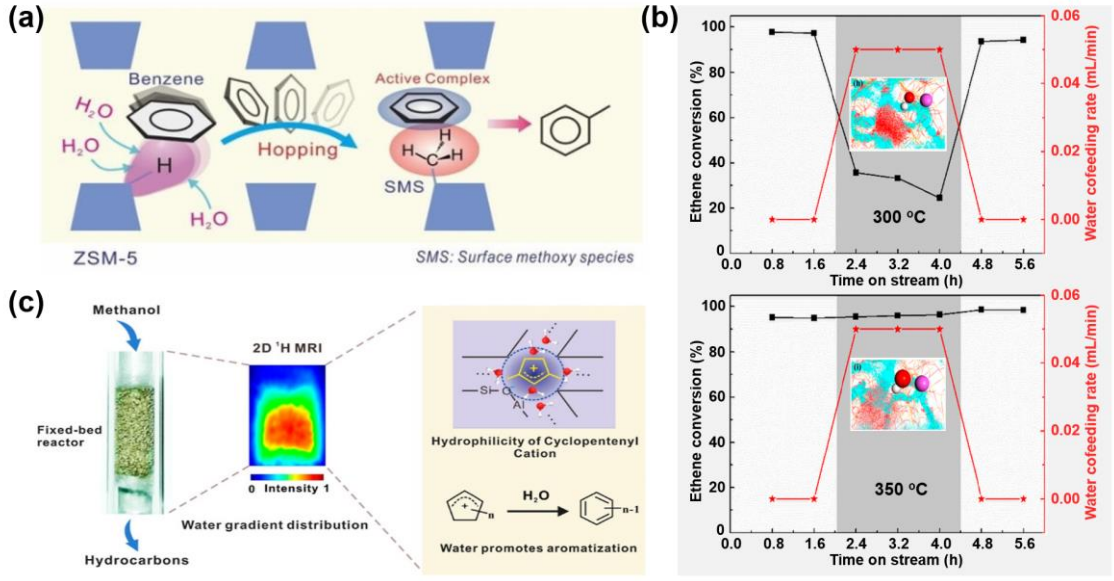

Fig. 11. (a) Schematic illustrating water driving benzene toward the surface methoxy species (SMS) to form the active SMS-benzene complex, promoting benzene methylation. Reprinted with permission from Ref. [13]. Copyright 2023, John Wiley and Sons. (b) Effects of water co-feeding on ethene conversion over H-ZSM-5 zeolite at 300 and 350 °C. Insets depict the density distributions of ethene and water around the BASs in H-ZSM-5 zeolite at both temperatures. The red and bluish clouds illustrate the adsorption probability distributions of water and ethene molecules, respectively. Reprinted with permission from Ref. [110]. Copyright 2020, American Chemical Society. (c) In the MTH reaction catalyzed by H-ZSM-5, the spatial distribution of hydrophilic cyclopentenyl cations, key intermediates, within the fixed-bed reactor generates a gradient distribution of adsorbed water along the axial positions, and the adsorbed water promotes the conversion of cyclopentenyl cations to aromatic compounds. Reprinted with permission from Ref. [117]. Copyright 2024, American Chemical Society.

n-hexadecane over Pt/MFI mesoporous zeolite. Recent studies by Wang *et al*. [13] revealed that competitive adsorption between water and benzene on BAS in H-ZSM-5 zeolite facilitates benzene reorientation within the channels and drives its adsorption onto SMS to form an SMS-benzene complex (Fig. 11(a)). At low water content (≤ 10 μL water), benzene methylation is promoted by the water-induced micro-hydrophobic effect, reaching a maximum conversion of 64.8% at 10 μL of water. However, excess water (> 10 μL water) inhibits benzene methylation by hydrating more reactive SMS into less reactive methanol and occupying more BASs near methanol, reducing the activity of both methanol and methanol-benzene complexes.

Notably, decreasing pressure and increasing temperature facilitate the desorption of water molecules from BAS, suggesting that the competitive adsorption effect induced by water molecules may be weakened in high-temperature catalytic reactions [12,23,110]. Wang *et al*. [110] systematically investigated the effect of water on ethene-to-aromatics conversion over H-ZSM-5 zeolite at 300–500 °C. At 300 °C, co-feeding water significantly reduced ethene conversion from 97.5% to 33%, while stopping the water co-feed quickly restored the conversion to 92% (Fig. 11(b) (top)). This is primarily due to water molecules preferentially adsorbing onto BASs to form Z–OH···H_2O hydrogen-bonded complexes and $H^+(H_2O)_n$ species, which occupy a large number of BASs and significantly inhibit ethene oligomerization, olefin-induced hydrogen transfer reaction, and hydrocarbon pool formation. However, at higher temperatures (≥ 350 °C), most adsorbed water molecules desorb and BAS recovers, making the competitive adsorption effect of water relatively insignificant (Fig. 11(b), bottom). Although water minimally affects ethene conversion under these conditions, physically adsorbed water still influences the propagation of the hydrocarbon pool by enhancing confinement, which in turn alters the distribution of aromatics. Recent studies by Liu *et al*. [116] showed that reaction temperatures above 240 °C enable the desorption of water interacting with the surface hydroxyl groups in H-MOR zeolite. This desorption avoids the poisoning effect of water on carbonylation active sites caused by competitive adsorption, thereby enhancing catalytic stability.

The interaction between water and hydrophilic intermediates during the reaction significantly affects water distribution within the zeolite pores, modulating reactivity and influencing reaction dynamics. Recently, Wang *et al*. [117] revealed the unique hydrophilic behavior of cyclopentenyl cations, essential intermediates in the MTH reaction, by utilizing micromagnetic resonance imaging (μMRI) and solid-state NMR techniques (Fig. 11(c)). By combining ^{13}C MAS NMR and 2D ^{1}H MRI, they observed that after methanol conversion at 300 °C for 30 min in a fixed-bed reactor, the upper layer (L1) of catalysts, which was characterized by more aromatic species (106.5 μmol/g) and fewer cyclopentenyl cations (53.6 μmol/g), exhibited poor water adsorption capacity. In contrast, the lower layer (L2), which contained abundant cyclopentenyl cations (135.2 μmol/g) and smaller aromatic species (10.4 μmol/g), exhibited strong water adsorption capacity. This behavior indicates that the polar cationic centers of cyclopentenyl cations initiate the

formation of water nucleus, resulting in a gradient distribution of adsorbed water along the axial positions in the fixed-bed reactor. This distribution aligns with the spatial distribution of the cyclopentenyl cations. Additionally, the nucleophilic nature of adsorbed water facilitates the deprotonation of cyclopentenyl cations to form cyclopentadiene, which subsequently undergoes ring expansion and dehydrogenation to generate methylbenzenes. As a result, these aromatic species enhance ethylene selectivity via the aromatic-based cycle.

3.1.2. *Stabilizing the ground and transition states*

In addition to competing for adsorption at active sites, water can also stabilize the adsorption ground state and transition state of key species within the confined spaces of molecular sieve catalysts. A recent study by Zhi *et al*. [118], combining DFT calculations and AIMD simulations, investigated the dehydration mechanism of 1-propanol over H-ZSM-5 zeolite in the presence of water. The findings revealed that the reduced dehydration rate is not attributed to competitive adsorption between 1-propanol and water, but rather to water's differential stabilization of the adsorbed 1-propanol species (both monomer and dimer) and the elimination transition state. In monomer-mediated dehydration, water stabilizes the adsorbed 1-propanol monomer more strongly (reducing enthalpy by 82 kJ/mol) than the elimination transition state (reducing enthalpy by 50 kJ/mol). This increases the activation barrier of the rate-limiting step, thereby slowing the propene formation rate. In dimer-mediated dehydration, water plays a similar role, but with a weaker effect, stabilizing both the adsorbed dimer and the elimination transition state to the same extent. Subsequently, Mei *et al*. [119] further explored the influence of water concentrations on the 1-propanol dehydration mechanism over H-ZSM-5 zeolite. Their findings also demonstrated that water stabilizes both the adsorption of 1-propanol monomers at BAS and protonated dimeric propanol complexes through hydrogen bonding with propanol molecules. The stabilizing effect intensifies with increasing water concentration, as evidenced by the adsorption energies: for 1-propanol monomers, –151 kJ/mol without water, –163 kJ/mol with two water molecules, and –188 kJ/mol with four; for protonated dimeric propanol complexes, –201 kJ/mol without water, –231 kJ/mol with two, and –294 kJ/mol with four. Gibbs free energy calculations further suggest that water-induced stabilization enables a kinetically favorable dehydration pathway to propene via a trimeric propanol-propanol-water complex, while making the unimolecular dehydration pathway less favorable.

In aqueous-phase reactions catalyzed by acidic zeolites, the presence of water leads to the formation of hydrated hydronium ions ($H_3O^+_{hydr.}$) within the zeolite pores, creating a unique ionic environment with specific local ionic strength [14,120]. This environment destabilizes the neutral adsorption ground state while stabilizing the charged transition state by increas-

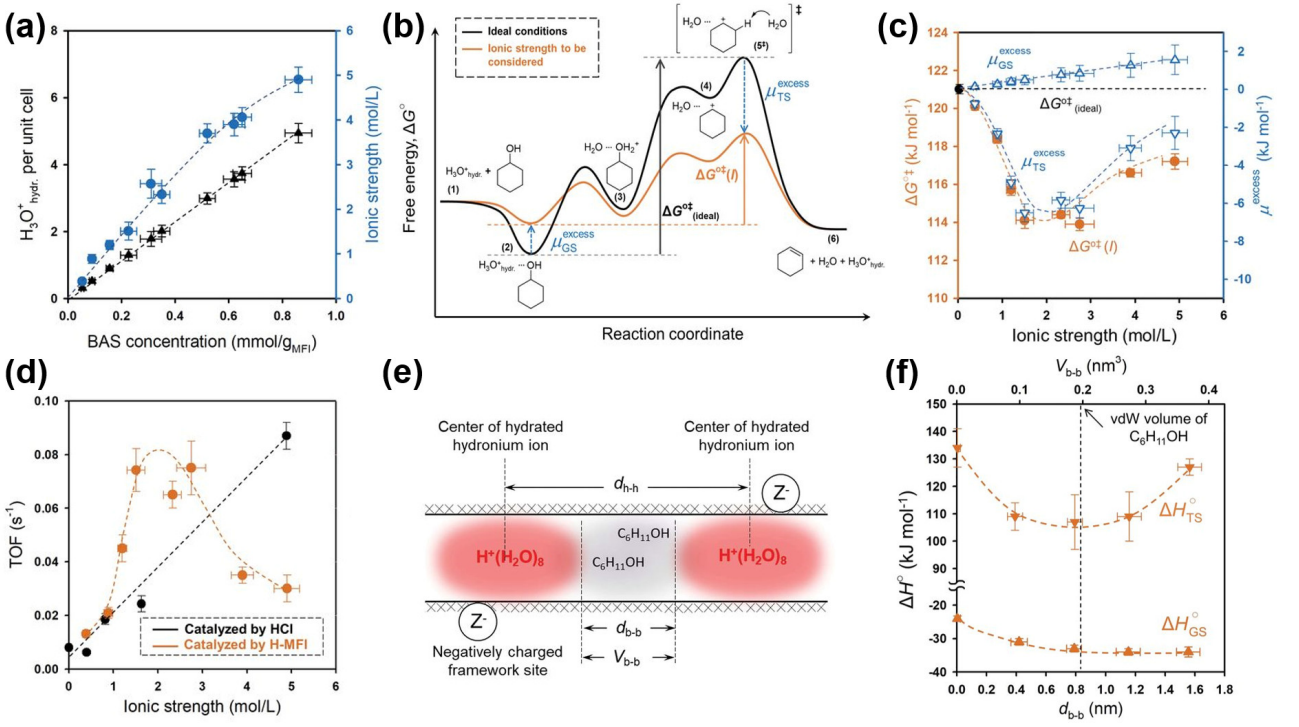

Fig. 12. (a) Unit cell-normalized concentrations of $H_3O^+_{hydr.}$ (triangles) and ionic strength (circles) as a function of BAS concentration. (b) Reaction steps and energy profiles for cyclohexanol dehydration catalyzed by $H_3O^+_{hydr.}$ in H-MFI zeolite under ideal and nonideal aqueous conditions. (c) Reaction free-energy barriers and excess chemical potential (μ^{excess}) of the ground state (GS) and transition state (TS) under the ideal condition and under an ionic strength. (d) TOF as a function of ionic strength under the catalysis of HCl (black) at 453 K and H-MFI (orange) at 423 K. (e) Schematic of $H_3O^+_{hydr.}$ and cyclohexanol in H-MFI micropore channels. (f) GS and TS enthalpies as a function of the mean distance ($d_{b\text{-}b}$) and volume ($V_{b\text{-}b}$) between the boundaries of neighboring $H_3O^+_{hydr.}$. Reprinted with permission from Ref. [14]. Copyright 2021, American Association for the Advancement of Science (AAAS).

ing and decreasing their excess chemical potentials (μ^{excess}), respectively. As a result, the activation free energy is lowered, thereby enhancing reaction rates. These zeolite-confined hydronium ions exhibit catalytic activity up to two orders of magnitude higher than that of unconfined hydronium ions in homogeneous aqueous acid solutions [121,122]. This effect was demonstrated in the aqueous-phase dehydration of cyclohexanol catalyzed by H-MFI zeolite [14]. The high local concentration of $H_3O^+_{hydr.}$ within H-MFI micropores induces a correspondingly high ionic strength, which increases monotonically with the BAS concentration (Fig. 12(a)) [14,35]. Notably, the reaction free-energy barrier is primarily reduced due to the stabilization of the charged transition state ($C_6H_{11}^+\cdots H_2O$) relative to the neutral ground state ($H_3O^+_{hydr.}\cdots C_6H_{11}OH$), as the μ^{excess} of the charged transition state is more sensitive to ionic strength (Figs. 12(b) and (c)) [14]. The energy barrier exhibits an inverse-volcano trend (Fig. 12(c)), with the lowest barrier occurring at an ionic strength of approximately 2 mol/L. Correspondingly, the turnover frequency (TOF) for cyclohexanol dehydration at 423 K increases to about 0.08 s^{-1} at an ionic strength of around 2 mol/L, but then decreases as ionic strength increases further (Fig. 12(d)). In contrast, in homogeneous HCl aqueous solutions at 453 K, the TOF positively correlates with ionic strength, exceeding 0.08 s^{-1} at an ionic strength of around 5 mol/L (Fig. 12(d)). The decrease in TOF at higher $H_3O^+_{hydr.}$ concentrations results from a strong van der Waals repulsion between $H_3O^+_{hydr.}$ and cyclohexanol within the H-MFI micropore channels, leading to an increase in the enthalpy of both the ground and transition states (Figs. 12(e) and (f)). A similar mechanism driven by $H_3O^+_{hydr.}$ ionic strength was also observed in the aqueous-phase cyclohexanol dehydration catalyzed by H-BEA zeolite. However, the increase in μ^{excess} of adsorbed cyclohexanol differs between the micropores of H-MFI (0.3–2.4 kJ/mol) and H-BEA (0.1–1.8 kJ/mol), leading to varying destabilization effects on the adsorbed cyclohexanol [36].

3.1.3. Proton transfer bridge

Due to their unique hydrogen-bonding network and polarity, water molecules can serve as proton transfer bridges participating in the elementary steps of catalytic reactions, such as MTO [12,123], alkane C–H bond activation [124], and direct oxidation of methane to methanol (DMTM) [125]. This role enhances the reaction rates of key steps, lowers activation energies, and further regulates reaction pathways and product distributions. Based on a first-principles kinetic study, Wispelaere *et al*. [123] analyzed the impact of water on the side-chain route for ethene and propene formation from hexamethylbenzene (HMB) in the MTO reaction over SAPO-34 at 670 K. The study revealed that water facilitates the deprotonation of alkyl groups by acting as a proton bridge between the ethyl-HMB/isopropyl-HMB complex and the acid site of the zeolite, thereby reducing the intrinsic free energy barrier for the elimination of ethene (E1, 99.3 kJ/mol) and propene (E2, 59.8 kJ/mol). Similarly, Zhang *et al*. [12] reported that water performs a comparable proton-transfer role in the naphthyl-based catalytic cycle for ethene and propene formation from 1,4-dimethylnaphthalene (1,4-DiMN) during methanol conversion over SAPO-34 at 773 K. Compared to the absence of water, its presence in the naphthyl-based catalytic cycle significantly reduced the free energy barriers and accelerated methylation (IM1, M2 and M3), deprotonation (DP1 and DP2), and elimination (E1 and E2) steps, as shown in Fig. 13(a). Water also activated protonated methanol molecules through hydrogen bonding, elongating the C–O bond from 1.44 to 1.47 Å (Fig. 13(b)), thereby enhancing methanol's reactivity in the methylation reaction. Moreover, they proposed a co-feeding strategy of water and methanol over a SAPO-34 catalyst pre-accommodated with naphthyl species, achieving an ethene selectivity of up to 67.5%.

Using D_2O isotopic tracer experiments and AIMD simulations, Xu *et al*. [125] revealed that water molecules directly participate in the N_2O-DMTM reaction over Cu-BEA zeolites through a proton transfer mechanism for the first time. Two water molecules can build a high-speed proton transfer bridge between CH_3^- and OH^- moieties at the $[Cu–O–Cu]^{2+}$ active site (Fig. 13(c)), facilitating methanol formation and desorption by overcoming remarkably low free energy barriers of 0.03 and 0.05 eV, respectively. Compared to water-free conditions, introducing 10 vol% water significantly enhances methanol selectivity (from 3.1% to 71.6%, Fig. 13(d)), productivity (from 16.8 to 242.9 μmol/(g_{cat}·h), Fig. 13(e)), and reaction stability (from 10 to 70 h). In addition, proton transfer driven by the "vehicle-hopping" mechanism, with individual H_2O or H_3O^+ molecules as carriers, was used to explain the enhancement of benzene C–H bond activation over H-ZSM-5 zeolite by the addition of sub-stoichiometric amounts of water at low pressure and room temperature, as reported by Chen *et al*. [124]. Interestingly, an increase in H/D exchange rates between benzene-d_6 and the BAS was observed only in H-ZSM-5 zeolite with high Al density (Si/Al = 15), and not in zeolites with low Al density (Si/Al = 40), suggesting that site proximity is crucial for proton transfer induced by water molecules. The rate was suppressed at high water loading due to competitive water adsorption on the BAS, preventing benzene from accessing the BAS. A similar rate inhibition at high water loading was observed in the activation of C–H bonds in isobutene [126]. Recently, Bocus *et al*. [127] utilized enhanced sampling AIMD simulations to investigate the role of water in the para protonation of ethylbenzene over H-ZSM-5 zeolite. When one water molecule is present per BAS, it acts as a proton transfer agent between the zeolite and ethylbenzene, lowering the protonation barrier from 76 ± 2 to 62 ± 3 kJ/mol and increasing the protonation rate by approximately one order of magnitude. However, increasing the water content to 3 or 6 molecules per BAS induces solvation, which strongly stabilizes the reactant state, increasing the barrier to 68 ± 2 and 72 ± 2 kJ/mol and causing the protonation rate enhancement to disappear.

3.2. Participation in reaction as a reactant

3.2.1. Reactions with intermediates or products

Water plays a crucial role not only through hydrogen-bond interactions but also as a reactant, reacting directly with inter-

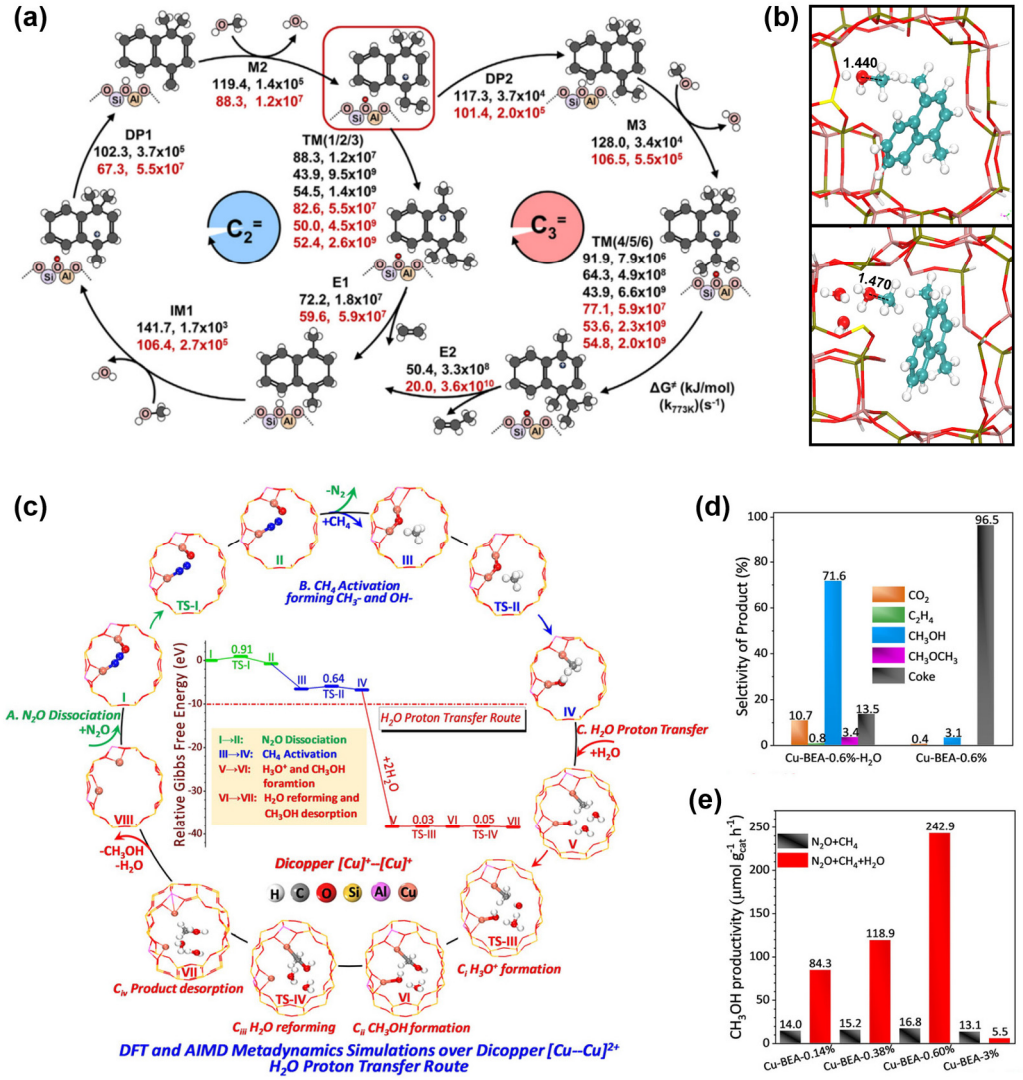

Fig. 13. (a) DFT-simulated methanol-to-olefins catalytic cycle via 1,4-DiMN over SAPO-34, showing Gibbs free energies and rate constants in the absence (black) and presence (red) of water at 773 K. (b) Optimized structures of the IM1 reactant without water and with water assistance. Reprinted with permission from Ref. [12]. Copyright 2024, Elsevier. (c) H_2O-assisted proton transfer route over a dicopper $[Cu]^+$–$[Cu]^+$ site in Cu-BEA. (d) CH_3OH productivities of Cu-BEA with different Cu loadings during N_2O-DMTM in the presence (red) and absence (black) of H_2O; reaction conditions: N_2O:CH_4:H_2O:He = 30:15:10(0):45(55), GHSV = 12000 h^{-1}, T = 320 °C. (e) Product selectivity of Cu-BEA-0.6% after 70 h of testing at 320 °C with and without H_2O. Reprinted with permission from Ref. [125]. Copyright 2021, John Wiley and Sons.

mediates and products formed during catalytic reactions to produce new substances, thereby altering reaction pathways, rates, and product selectivity [128,129]. Recently, Bollini *et al*. [129] employed DFT calculations and transient stoichiometric experiments to show that co-fed water reacts with formaldehyde (HCHO), which is a crucial intermediate in MTO, to produce methanediol ($CH_2(OH)_2$) on H-SSZ-13 zeolite. Unlike $CH_2(OH)_2$, HCHO participates in initiating (promoting hydrocarbon pool buildup) and terminating (causing catalyst deactivation) MTO chain propagation cycles, and its hydrolysis decreases chain initiation and termination rates while simultaneously increasing total turnovers. In particular, some important intermediates (*e.g.*, alkoxy and acyl groups) exhibit high reactivity with water during catalytic processes, garnering significant attention. For example, in the DME carbonylation reaction, water is highly detrimental to methyl acetate formation by reacting with surface active species [130]. Specifically, water strongly adsorbs onto surface methoxy groups (SMS) formed by DME activation at the BAS, producing methanol as a byproduct. This significantly decreases the reactivity of SMS toward CO, thereby inhibiting the formation of acetyl groups, which are key precursors to methyl acetate. Similarly, surface acetyl species can be hydrolyzed to form acetic acid during the zeolite-catalyzed methyl acetate-to-hydrocarbon (MATH) conversion [128].

3.2.2. *Regeneration of coke-deactivated catalysts via steam gasification*

In industrial processes such as petrochemical and coal chemical reactions catalyzed by molecular sieves, catalyst de-

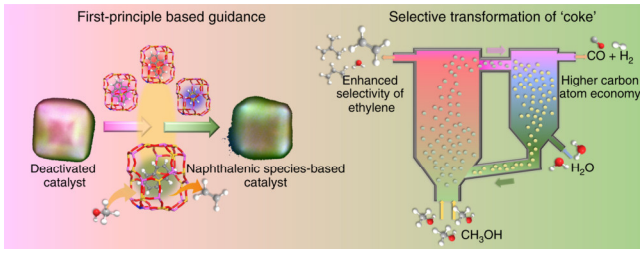

Fig. 14. Selective transformation of coke into specific naphthalenic species over deactivated SAPO-34 catalysts. Reprinted with permission from Ref. [132]. Copyright 2021, Springer Nature.

activation caused by coke deposition is inevitable. Steam gasification has proven to be an effective strategy for regenerating deactivated catalysts, transforming coke species into valuable syngas (CO and H_2) while simultaneously restoring catalytic activity [131]. Compared to coke oxidation using air or oxygen as the regeneration gas, steam gasification also significantly reduces CO_2 emissions. In the MTO reaction, partial regeneration of deactivated SAPO-34 catalysts by steam gasification results in higher ethylene selectivity than air combustion, owing to the presence of hydrocarbon pool (HCP) species, such as methylated benzenes and naphthalene, in the residual coke [132,133]. A recent study by Zhou *et al*. [132] reported that coke species within deactivated SAPO-34 catalyst were selectively transformed to active naphthalene species via steam cracking at 953 K (Fig. 14). These naphthalene species confined within the CHA cavity of SAPO-34, exhibit remarkable stability at high temperature and promote ethylene formation through naphthalene-based catalytic cycle. The effectiveness of this coke transformation strategy was evaluated through pilot experiments in a fluidized bed reactor-regenerator under industrial-like continuous operations, achieving an unexpectedly high light olefin selectivity of 85%, while producing 88% valuable CO and H_2 and only 5% CO_2 as byproducts from regeneration (Fig. 14). This strategy effectively regulates the MTO reaction by partially gasifying coke species with steam, which reduces CO_2 emissions and enhances carbon atom utilization, thereby further boosting the economic viability and sustainability of the MTO process.

Later, Wang *et al*. [134] utilized steam cracking to selectively eliminate naphthalenic species formed by ethylene precoking at the SAPO-34 crystal rim, due to the steric hindrance effect, while retaining those within the crystal center. This combined strategy of precoking and steaming, which directionally constructs active naphthalenic species within the SAPO-34 crystal center, was applied to commercial SAPO-34 catalysts, achieving a high total selectivity of approximately 90% for ethylene and propylene, while prolonging the catalyst's lifetime by 2.5-fold. Notably, precoking efficiently protects the SAPO-34 framework against the irreversible hydrolysis of T–O–T bonds, thereby enhancing its long-term stability in the presence of water [100]. Very recently, Wang *et al*. [108] employed high-resolution matrix-assisted laser desorption/ionization Fourier-transform ion cyclotron resonance mass spectrometry (MALDI FT-ICR MS) to investigate the decomposition pathway of cross-linked cage-passing polycyclic aromatic hydrocarbons (PAHs) during high-temperature steam regeneration of SAPO-34 catalysts in the MTO process. These cage-passing PAHs species are formed through the direct coupling of in-cage HCP species. Under regeneration conditions, water promotes their decomposition into in-cage HCP species by selectively cracking the inter-cage local structures at the 8-membered rings, followed by deep aromatic steam reforming, which simultaneously produces valuable H_2 and CO as the main products.

4. Conclusions and perspectives

Herein, we review the complex host-guest interactions between aluminosilicate zeolites/SAPO molecular sieves and water, as well as the multifaceted roles of water in catalysis. Water significantly influences both the molecular sieve framework and the reaction network during the catalysis process. It can induce various dynamic structural changes, including water adsorption at active sites, reversible and irreversible hydrolysis of T–O–T bonds, resulting from interactions ranging from weak to strong. These interactions are closely dependent on factors including temperature, water content and phase, as well as the composition and topology of molecular sieves. While reversible hydrolysis of T–O–T bonds does not cause framework degradation, irreversible breakage can lead to structural changes, such as defect formation, dealumination, desilication, mesopore/macropore generation, and even structural collapse. These water-induced reversible and irreversible structural changes significantly affect the adsorption and diffusion behaviors of guest molecules (reactants, intermediates, and products). Additionally, water, as a reactant, product, or medium, participates in the complex catalytic network, influencing reaction kinetics and catalytic performance either via hydrogen bonding interactions or through direct reactions with other guest molecules. These water-induced effects can be either beneficial or detrimental, but are tunable through careful control of reaction conditions such as temperature, pressure, and water content.

Current studies primarily focus on water-molecular sieve interactions but rarely address the role of coexisting guest molecules. In real catalytic reactions, guest molecules (*e.g.*, reactants, intermediates, and products) not only interact with molecular sieve framework but also with water molecules, thus altering the water-molecular sieve interactions. Future research should therefore aim to elucidate the water-induced reversible or irreversible dynamic evolution of the molecular sieve framework, especially active sites, under real catalytic reaction conditions to establish accurate structure-activity relationships. The potential effects of reversible hydrolysis of framework T–O–T bonds (*i.e.*, their rapid and reversible cleavage and reformation) warrant attention, as this dynamic process may modulate the pore microenvironment and framework flexibility, thereby influencing the adsorption, diffusion, and transformation of reactants and intermediates. Moreover, understanding the influence of water molecules on the diffusion behavior of reactants, intermediates, and products within zeolite channels remains a significant challenge. Addressing this will require integrated studies that consider the interplay

among water, guest molecules, and the molecular sieve framework. Advanced characterization techniques and theoretical calculations are essential to unraveling these complex catalytic interactions and addressing their relevance. Since most characterization techniques are performed under vacuum or inert gas environments, the real water structures and their dynamic behaviors in zeolite pores remain unclear under reaction conditions. To gain deeper insights, it is crucial to develop *in-situ* and *operando* characterization techniques with higher temporal and spatial resolution to capture the real-time behavior of water molecules, such as their adsorption sites, local structures, diffusion paths, spatial distribution, as well as hydrogen-bond networks and proton transfer pathways mediated by water molecules. Complementary theoretical approaches such as AIMD, DFT, MD, and Monte Carlo (MC) simulations are also imperative to elucidate the roles of water in molecular sieve catalysis at the molecule level. A deeper understanding of the interplay among water, guest molecules, and molecular sieves will provide theoretical foundations for the rational design of molecular sieve catalysts with high activity and stability, as well as for the optimization of water-involved reactions.

References

[1] E. T. C. Vogt, B. M. Weckhuysen, *Chem. Soc. Rev.*, **2015**, 44, 7342–7370.
[2] A. Galadima, O. Muraza, *J. Ind. Eng. Chem.*, **2018**, 61, 265–280.
[3] Y. Wu, J. Han, W. Zhang, Z. Yu, K. Wang, X. Fang, Y. Wei, Z. Liu, *J. Am. Chem. Soc.*, **2024**, 146, 8086–8097.
[4] D. Liu, L. Cao, G. Zhang, L. Zhao, J. Gao, C. Xu, *Fuel Process. Technol.*, **2021**, 216, 106770.
[5] R. Liu, X. Shao, C. Wang, W. Dai, N. Guan, *Chin. J. Catal.*, **2023**, 47, 67–92.
[6] S. Wang, Z. Qin, M. Dong, J. Wang, W. Fan, *Chem Catal.*, **2022**, 2, 1657–1685.
[7] S. Lin, H. Li, P. Tian, Y. Wei, M. Ye, Z. Liu, *J. Am. Chem. Soc.*, **2025**, 147, 11585–11607.
[8] J. Niu, X. Ding, S. Xu, Y. Wei, Z. Liu, *Chem. Soc. Rev.*, **2025**, 54, 6652–6696.
[9] T. Ennaert, J. Van Aelst, J. Dijkmans, R. De Clercq, W. Schutyser, M. Dusselier, D. Verboekend, B. F. Sels, *Chem. Soc. Rev.*, **2016**, 45, 584–611.
[10] C. J. Heard, L. Grajciar, F. Uhlík, M. Shamzhy, M. Opanasenko, J. Čejka, P. Nachtigall, *Adv. Mater.*, **2020**, 32, 2003264.
[11] R. Simancas, A. Chokkalingam, S. P. Elangovan, Z. Liu, T. Sano, K. Iyoki, T. Wakihara, T. Okubo, *Chem. Sci.*, **2021**, 12, 7677–7695.
[12] C. Zhang, X. Wu, Y. Zhang, W. Zhang, S. Lin, C. Lou, S. Xu, D. He, L. Wang, Y. Wei, Z. Liu, *Chem Catal.*, **2024**, 4, 101025.
[13] C. Wang, Y. Chu, D. Xiong, H. Wang, M. Hu, Q. Wang, J. Xu, F. Deng, *Angew. Chem. Int. Ed.*, **2024**, 63, e202313974.
[14] N. Pfriem, P. H. Hintermeier, S. Eckstein, S. Kim, Q. Liu, H. Shi, L. Milakovic, Y. Liu, G. L. Haller, E. Baráth, Y. Liu, J. A. Lercher, *Science*, **2021**, 372, 952–957.
[15] D. E. Resasco, S. P. Crossley, B. Wang, J. L. White, *Catal. Rev.*, **2021**, 63, 302–362.
[16] K. Stanciakova, B. M. Weckhuysen, *Trends Chem.*, **2021**, 3, 456–468.
[17] Z.-P. Hu, J. Han, Y. Wei, Z. Liu, *ACS Catal.*, **2022**, 12, 5060–5076.
[18] Q. Liu, J. A. van Bokhoven, *Chem. Soc. Rev.*, **2024**, 53, 3065–3095.
[19] G. Li, B. Wang, D. E. Resasco, *ACS Catal.*, **2020**, 10, 1294–1309.
[20] L. Lin, Y. Ge, H. Zhang, M. Wang, D. Xiao, D. Ma, *JACS Au*, **2021**, 1, 1834–1848.
[21] T. Sun, S. Xu, D. Xiao, Z. Liu, G. Li, A. Zheng, W. Liu, Z. Xu, Y. Cao, Q. Guo, N. Wang, Y. Wei, Z. Liu, *Angew. Chem. Int. Ed.*, **2020**, 59, 20672–20681.
[22] M. Ravi, V. L. Sushkevich, J. A. van Bokhoven, *Nat. Mater.*, **2020**, 19, 1047–1056.
[23] J. H. Hack, J. P. Dombrowski, X. Ma, Y. Chen, N. H. C. Lewis, W. B. Carpenter, C. Li, G. A. Voth, H. H. Kung, A. Tokmakoff, *J. Am. Chem. Soc.*, **2021**, 143, 10203–10213.
[24] A. Vjunov, M. Wang, N. Govind, T. Huthwelker, H. Shi, D. Mei, J. L. Fulton, J. A. Lercher, *Chem. Mater.*, **2017**, 29, 9030–9042.
[25] M. Wang, N. R. Jaegers, M.-S. Lee, C. Wan, J.-Z. Hu, H. Shi, D. Mei, S. D. Burton, D. M. Camaioni, O. Y. Gutiérrez, V.-A. Glezakou, R. Rousseau, Y. Wang, J. A. Lercher, *J. Am. Chem. Soc.*, **2019**, 141, 3444–3455.
[26] K. Chen, J. Kelsey, J. L. White, L. Zhang, D. Resasco, *ACS Catal.*, **2015**, 5, 7480–7487.
[27] K. Gong, F. Jiao, Y. Chen, X. Liu, X. Pan, X. Han, X. Bao, G. Hou, *J. Phys. Chem. C*, **2019**, 123, 17368–17374.
[28] E. Grifoni, G. Piccini, J. A. Lercher, V.-A. Glezakou, R. Rousseau, M. Parrinello, *Nat. Commun.*, **2021**, 12, 2630.
[29] J. Randrianandraina, M. Badawi, B. Cardey, M. Grivet, J.-E. Groetz, C. Ramseyer, F. T. Anzola, C. Chambelland, D. Ducret, *Phys. Chem. Chem. Phys.*, **2021**, 23, 19032–19042.
[30] F. Wakabayashi, J. N. Kondo, K. Domen, C. Hirose, *J. Phys. Chem.*, **1996**, 100, 1442–1444.
[31] L. Marchese, J. Chen, P. A. Wright, J. M. Thomas, *J. Phys. Chem.*, **1993**, 97, 8109–8112.
[32] L. Smith, A. K. Cheetham, R. E. Morris, L. Marchese, J. M. Thomas, P.

Graphical Abstract

Chin. J. Catal., 2025, 79: 9–31 doi: 10.1016/S1872-2067(25)64828-5

Water interactions in molecular sieve catalysis: Framework evolution and reaction modulation

Linhai He, Caiyi Lou, Lu Sun, Jing Niu, Shutao Xu *, Yingxu Wei, Zhongmin Liu *
Dalian Institute of Chemical Physics, Chinese Academy of Sciences; University of Chinese Academy of Sciences

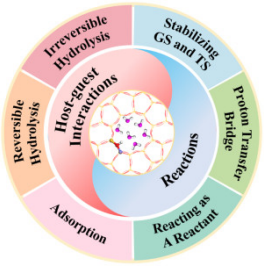

This review discusses the current understanding of the interactions between water and molecular sieves, as well as the roles of water in molecular sieve catalysis, providing valuable insights for optimizing catalytic performance in water-involved reactions.

A. Wright, J. Chen, *Science*, **1996**, 271, 799–802.
[33] M. Krossner, J. Sauer, *J. Phys. Chem.*, **1996**, 100, 6199–6211.
[34] M. V. Vener, X. Rozanska, J. Sauer, *Phys. Chem. Chem. Phys.*, **2009**, 11, 1702–1712.
[35] S. Eckstein, P. H. Hintermeier, R. Zhao, E. Baráth, H. Shi, Y. Liu, J. A. Lercher, *Angew. Chem. Int. Ed.*, **2019**, 58, 3450–3455.
[36] S. Kim, N. R. Jaegers, W. Hu, J.-Z. Hu, F. Chen, Q. Liu, D. M. Camaioni, M. A. Derewinski, O. Y. Gutiérrez, Y. Liu, J. A. Lercher, *J. Phys. Chem. C*, **2023**, 127, 23390–23399.
[37] M. Iwamoto, S. Morita, S. Kagawa, *J. Phys. Chem.*, **1981**, 85, 3955–3957.
[38] R. Von Ballmoos, W. M. Meier, *J. Phys. Chem.*, **1982**, 86, 2698–2700.
[39] L. M. Bull, A. K. Cheetham, *17O NMR Studies of Siliceous Faujasite*, Elsevier,**1997**, 471–477.
[40] Z. Xu, J. F. Stebbins, *Geochim. Cosmochim. Acta*, **1998**, 62, 1803–1809.
[41] N. Mizuno, H. Mori, K. Mineo, M. Iwamoto, *J. Phys. Chem. B*, **1999**, 103, 10393–10399.
[42] C. J. Heard, L. Grajciar, C. M. Rice, S. M. Pugh, P. Nachtigall, S. E. Ashbrook, R. E. Morris, *Nat. Commun.*, **2019**, 10, 4690.
[43] S. M. Pugh, P. A. Wright, D. J. Law, N. Thompson, S. E. Ashbrook, *J. Am. Chem. Soc.*, **2020**, 142, 900–906.
[44] K. Chen, A. Zornes, V. Nguyen, B. Wang, Z. Gan, S. P. Crossley, J. L. White, *J. Am. Chem. Soc.*, **2022**, 144, 16916–16929.
[45] Y. Ji, K. Chen, X. Han, X. Bao, G. Hou, *J. Am. Chem. Soc.*, **2024**, 146, 11211–11224.
[46] T. Benešov, M. Liu, P. Nachtigall, C. J. Heard, *Microporous Mesoporous Mater.*, **2024**, 368, 113007.
[47] S. Prodinger, H. Shi, S. Eckstein, J.-Z. Hu, M. V. Olarte, D. M. Camaioni, M. A. Derewinski, J. A. Lercher, *Chem. Mater.*, **2017**, 29, 7255–7262.
[48] D. T. Bregante, M. C. Chan, J.-Z. Tan, E. Z. Ayla, C. P. Nicholas, D. Shukla, D. W. Flaherty, *Nat. Catal.*, **2021**, 4, 797–808.
[49] B. Fan, D. Zhu, L. Wang, S. Xu, Y. Wei, Z. Liu, *Inorg. Chem. Front.*, **2022**, 9, 3609–3618.
[50] L. Zhang, K. Chen, B. Chen, J. L. White, D. E. Resasco, *J. Am. Chem. Soc.*, **2015**, 137, 11810–11819.
[51] S. Prodinger, H. Shi, H. Wang, M. A. Derewinski, J. A. Lercher, *Appl. Catal. B*, **2018**, 237, 996–1002.
[52] L. He, J. Niu, S. Han, D. Fan, W. Zhang, S. Xu, Y. Wei, Z. Liu, *ChemCatChem*, **2024**, 16, e202401270.
[53] L.-H. He, J.-J. Li, S.-Y. Han, D. Fan, X.-J. Li, S.-T. Xu, Y.-X. Wei, Z.-M. Liu, *Chem. Synth.*, **2024**, 4, 1.
[54] G. N. Kalantzopoulos, F. Lundvall, K. Thorshaug, A. Lind, P. Vajeeston, I. Dovgaliuk, B. Arstad, D. S. Wragg, H. Fjellvåg, *Chem. Mater.*, **2020**, 32, 1495–1505.
[55] C. Wang, S. Leng, H. Guo, L. Cao, J. Huang, *Appl. Surf. Sci.*, **2019**, 478, 319–326.
[56] J. Holzinger, P. Beato, L. F. Lundegaard, J. Skibsted, *J. Phys. Chem. C*, **2018**, 122, 15595–15613.
[57] Y. Wang, P. Guerra, A. Zaker, A. R. Maag, G. A. Tompsett, L. J. Smith, X. Huang, J. Q. Bond, M. T. Timko, *ACS Catal.*, **2020**, 10, 6623–6634.
[58] K. Miyake, R. Inoue, T. Miura, M. Nakai, H. Al-Jabri, Y. Hirota, Y. Uchida, S. Tanaka, M. Miyamoto, S. Inagaki, Y. Kubota, C.-Y. Kong, N. Nishiyama, *Microporous Mesoporous Mater.*, **2019**, 288, 109523.
[59] S. Prodinger, M. A. Derewinski, A. Vjunov, S. D. Burton, I. Arslan, J. A. Lercher, *J. Am. Chem. Soc.*, **2016**, 138, 4408–4415.
[60] K. Iyoki, K. Kikumasa, T. Onishi, Y. Yonezawa, A. Chokkalingam, Y. Yanaba, T. Matsumoto, R. Osuga, S. P. Elangovan, J. N. Kondo, A. Endo, T. Okubo, T. Wakihara, *J. Am. Chem. Soc.*, **2020**, 142, 3931–3938.
[61] Y. Zhao, J. Liu, G. Xiong, H. Guo, *Chin. J. Catal.*, **2017**, 38, 138–145.
[62] Y. Chu, X. Gao, X. Zhang, G. Xu, G. Li, A. Zheng, *Phys. Chem. Chem. Phys.*, **2018**, 20, 11702–11712.
[63] J. Sun, H. Fang, P. I. Ravikovitch, D. S. Sholl, *J. Phys. Chem. C*, **2020**, 124, 668–676.
[64] M. Chen, W. Zhao, Y. Wei, S.-B. Ren, Y. Chen, D. Mei, D.-M. Han, J. Yu, *Chem. Sci.*, **2024**, 15, 5548–5554.
[65] X. Ding, C. Liu, J. Niu, N. Chen, S. Xu, Y. Wei, Z. Liu, *Chin. J. Struct. Chem.*, **2024**, 43, 100247.
[66] S. Malola, S. Svelle, F. L. Bleken, O. Swang, *Angew. Chem. Int. Ed.*, **2012**, 51, 652–655.
[67] M.-C. Silaghi, C. Chizallet, E. Petracovschi, T. Kerber, J. Sauer, P. Raybaud, *ACS Catal.*, **2015**, 5, 11–15.
[68] M.–C. Silaghi, C. Chizallet, J. Sauer, P. Raybaud, *J. Catal.*, **2016**, 339, 242–255.
[69] P. Liu, Q. Liu, D. Mei, *J. Phys. Chem. C*, **2021**, 125, 24613–24621.
[70] K. Stanciakova, B. Ensing, F. Göltl, R. E. Bulo, B. M. Weckhuysen, *ACS Catal.*, **2019**, 9, 5119–5135.
[71] M. Nielsen, A. Hafreager, R. Y. Brogaard, K. De Wispelaere, H. Falsig, P. Beato, V. Van Speybroeck, S. Svelle, *Catal. Sci. Technol.*, **2019**, 9, 3721–3725.
[72] M. Nielsen, R. Y. Brogaard, H. Falsig, P. Beato, O. Swang, S. Svelle, *ACS Catal.*, **2015**, 5, 7131–7139.
[73] K. Chen, Z. Gan, S. Horstmeier, J. L. White, *J. Am. Chem. Soc.*, **2021**, 143, 6669–6680.
[74] K. Chen, S. Horstmeier, V. T. Nguyen, B. Wang, S. P. Crossley, T. Pham, Z. Gan, I. Hung, J. L. White, *J. Am. Chem. Soc.*, **2020**, 142, 7514–7523.
[75] Z. Wang, D. Xiao, K. Chen, C. Lou, L. Liang, S. Xu, G. Hou, *ACS Catal.*, **2023**, 13, 4960–4970.
[76] X. Bai, J. Zhang, C. Liu, S. Xu, Y. Wei, Z. Liu, *Microporous Mesoporous Mater.*, **2023**, 354, 112555.
[77] M. Zheng, Q. Wang, Y. Chu, X. Tan, Postech, W. Huang, Y. Xi, Y. Wang, G. Qi, J. Xu, S. B. Hong, Postech, F. Deng, *J. Am. Chem. Soc.*, **2024**, 146, 29417–29428.
[78] C. Liu, G. Li, E. J. M. Hensen, E. A. Pidko, *ACS Catal.*, **2015**, 5, 7024–7033.
[79] X. Yi, K. Liu, W. Chen, J. Li, S. Xu, C. Li, Y. Xiao, H. Liu, X. Guo, S.-B. Liu, A. Zheng, *J. Am. Chem. Soc.*, **2018**, 140, 10764–10774.
[80] Z. Yu, S. Li, Q. Wang, A. Zheng, X. Jun, L. Chen, F. Deng, *J. Phys. Chem. C*, **2011**, 115, 22320–22327.
[81] Z. Yu, A. Zheng, Q. Wang, L. Chen, J. Xu, J.-P. Amoureux, F. Deng, *Angew. Chem. Int. Ed.*, **2010**, 49, 8657–8661.
[82] T. N. Pham, V. Nguyen, B. Wang, J. L. White, S. Crossley, *ACS Catal.*, **2021**, 11, 6982–6994.
[83] S. Zhao, W. Yang, K. D. Kim, L. Wang, Z. Wang, R. Ryoo, J. Huang, *J. Phys. Chem. C*, **2021**, 125, 11665–11676.
[84] X. Wang, Q. Wang, C. Wang, Y. Chu, M. Hu, F. Deng, J. Yu, J. Xu, *J. Am. Chem. Soc.*, **2025**, 147, 17829–17838.
[85] A. K. Jamil, O. Muraza, R. Osuga, E. N. Shafei, K.-H. Choi, Z. H. Yamani, A. Somali, T. Yokoi, *J. Phys. Chem. C*, **2016**, 120, 22918–22926.
[86] R. M. Ravenelle, F. Schüßler, A. D'Amico, N. Danilina, J. A. van Bokhoven, J. A. Lercher, C. W. Jones, C. Sievers, *J. Phys. Chem. C*, **2010**, 114, 19582–19595.
[87] A. R. Maag, G. A. Tompsett, J. Tam, C. A. Ang, G. Azimi, A. D. Carl, X. Huang, L. J. Smith, R. L. Grimm, J. Q. Bond, M. T. Timko, *Phys. Chem. Chem. Phys.*, **2019**, 21, 17880–17892.
[88] A. Vjunov, J. L. Fulton, D. M. Camaioni, J. Z. Hu, S. D. Burton, I. Arslan, J. A. Lercher, *Chem. Mater.*, **2015**, 27, 3533–3545.
[89] A. Buchholz, W. Wang, A. Arnold, M. Xu, M. Hunger, *Microporous Mesoporous Mater.*, **2003**, 57, 157–168.
[90] B. Parlitz, U. Lohse, E. Schreier, *Microporous Mater.*, **1994**, 2,

223–228.
[91] H.-L. Zubowa, E. Alsdorf, R. Fricke, F. Neissendorfer, J. Richter-Mendau, E. Schreier, D. Zeigan, B. Zibrowius, *J. Chem. Soc., Faraday Trans.*, **1990**, 86, 2307–2312.
[92] J. P. Lourenço, M. F. Ribeiro, F. R. Ribeiro, J. Rocha, Z. Gabelica, E. G. Derouane, *Microporous Mater.*, **1995**, 4, 445–453.
[93] R. Vomscheid, M. Briend, M. J. Peltre, P. Massiani, P. P. Man, D. Barthomeuf, *J. Chem. Soc., Chem. Commun.*, **1993**, 544–546.
[94] B. Arstad, A. Lind, J. H. Cavka, K. Thorshaug, D. Akporiaye, D. Wragg, H. Fjellvåg, A. Grønvold, T. Fuglerud, *Microporous Mesoporous Mater.*, **2016**, 225, 421–431.
[95] M. Briend, R. Vomscheid, M. J. Peltre, P. P. Man, D. Barthomeuf, *J. Phys. Chem.*, **1995**, 99, 8270–8276.
[96] J. Bauer, T. Selvam, J. Ofili, E. Che, R. Herrmann, W. Schwieger, *Stability of AlPO and SAPO Molecular Sieves During Adsorption-Desorption Cycles of Water Vapor Investigated by in-situ XRD Measurements*, Elsevier, **2007**, 837–844.
[97] T. Fjermestad, S. Svelle, O. Swang, *J. Phys. Chem. C*, **2013**, 117, 13442–13451.
[98] T. Fjermestad, S. Svelle, O. Swang, *J. Phys. Chem. C*, **2015**, 119, 2073–2085.
[99] T. Fjermestad, S. Svelle, O. Swang, *J. Phys. Chem. C*, **2015**, 119, 2086–2095.
[100] L. Yang, C. Wang, L. Zhang, W. Dai, Y. Chu, J. Xu, G. Wu, M. Gao, W. Liu, Z. Xu, P. Wang, N. Guan, M. Dyballa, M. Ye, F. Deng, W. Fan, L. Li, *Nat. Commun.*, **2021**, 12, 4661.
[101] C. Wang, A. Brenig, J. Xu, F. Deng, V. Paunović, J. A. van Bokhoven, *J. Am. Chem. Soc.*, **2024**, 146, 34279–34284.
[102] K. De Wispelaere, C. S. Wondergem, B. Ensing, K. Hemelsoet, E. J. Meijer, B. M. Weckhuysen, V. Van Speybroeck, J. Ruiz-Martínez, *ACS Catal.*, **2016**, 6, 1991–2002.
[103] C. Zhang, X. Wu, Y. Zhang, L. Wang, Y. Jin, M. Gao, M. Ye, Y. Wei, Z. Liu, *ACS Catal.*, **2025**, 15, 1553–1562.
[104] M. Luo, Y. Fu, B. Hu, D. Wang, B. Wang, G. Mao, *Appl. Catal. A*, **2019**, 570, 209–217.
[105] X. Zhao, J. Li, P. Tian, L. Wang, X. Li, S. Lin, X. Guo, Z. Liu, *ACS Catal.*, **2019**, 9, 3017–3025.
[106] T. Shoinkhorova, T. Cordero-Lanzac, A. Ramirez, S.-H. Chung, A. Dokania, J. Ruiz-Martinez, J. Gascon, *ACS Catal.*, **2021**, 11, 3602–3613.
[107] J. Valecillos, I. Hita, E. Sastre, A. T. Aguayo, P. Castaño, *ChemCatChem*, **2021**, 13, 3140–3154.
[108] N. Wang, L. Wang, Y. Zhi, J. Han, C. Zhang, X. Wu, J. Zhang, L. Wang, B. Fan, S. Xu, Y. Zheng, S. Lin, R. Wu, Y. Wei, Z. Liu, *J. Energy Chem.*, **2023**, 76, 105–116.
[109] S. Lin, Y. Zhi, W. Zhang, X. Yuan, C. Zhang, M. Ye, S. Xu, Y. Wei, Z. Liu, *Chin. J. Catal.*, **2023**, 46, 11–27.
[110] H. Wang, Y. Hou, W. Sun, Q. Hu, H. Xiong, T. Wang, B. Yan, W. Qian, *ACS Catal.*, **2020**, 10, 5288–5298.
[111] J. Valecillos, G. Elordi, A. T. Aguayo, P. Castaño, *Catal. Sci. Technol.*, **2021**, 11, 1269–1281.
[112] C. J. Baranowski, T. Fovanna, M. Roger, M. Signorile, J. McCaig, A. M. Bahmanpour, D. Ferri, O. Kröcher, *ACS Catal.*, **2020**, 10, 8106–8119.
[113] Y. Chen, X. Ma, J. H. Hack, S. Zhang, A. Peng, J. P. Dombrowski, G. A. Voth, A. Tokmakoff, M. C. Kung, H. H. Kung, *J. Am. Chem. Soc.*, **2024**, 146, 10342–10356.
[114] R. Brosius, P. J. Kooyman, J. C. Q. Fletcher, *ACS Catal.*, **2016**, 6, 7710–7715.
[115] J. Gil-Coba, S. C. Marie-Rose, J.-M. Lavoie, *Catal. Lett.*, **2016**, 146, 2534–2542.
[116] S. Liu, G. Wu, Y. Chen, Y. Han, M. Zhang, J. Kang, M. Tang, K. P. de Jong, Q. Zhang, Y. Wang, K. Cheng, *AlChE J.*, **2025**, 71, e18664.
[117] C. Wang, M. Zheng, M. Hu, W. Cai, Y. Chu, Q. Wang, J. Xu, F. Deng, *J. Am. Chem. Soc.*, **2024**, 146, 8688–8696.
[118] Y. Zhi, H. Shi, L. Mu, Y. Liu, D. Mei, D. M. Camaioni, J. A. Lercher, *J. Am. Chem. Soc.*, **2015**, 137, 15781–15794.
[119] D. Mei, J. A. Lercher, *AlChE J.*, **2017**, 63, 172–184.
[120] L. Milaković, P. H. Hintermeier, Y. Liu, E. Baráth, J. A. Lercher, *Angew. Chem. Int. Ed.*, **2021**, 60, 24806–24810.
[121] Y. Liu, A. Vjunov, H. Shi, S. Eckstein, D. M. Camaioni, D. Mei, E. Baráth, J. A. Lercher, *Nat. Commun.*, **2017**, 8, 14113.
[122] H. Shi, S. Eckstein, A. Vjunov, D. M. Camaioni, J. A. Lercher, *Nat. Commun.*, **2017**, 8, 15442.
[123] K. De Wispelaere, K. Hemelsoet, M. Waroquier, V. Van Speybroeck, *J. Catal.*, **2013**, 305, 76–80.
[124] K. Chen, A. Gumidyala, M. Abdolrhamani, C. Villines, S. Crossley, J. L. White, *J. Catal.*, **2017**, 351, 130–135.
[125] R. Xu, N. Liu, C. Dai, Y. Li, J. Zhang, B. Wu, G. Yu, B. Chen, *Angew. Chem. Int. Ed.*, **2021**, 60, 16634–16640.
[126] K. Chen, J. Damron, C. Pearson, D. Resasco, L. Zhang, J. L. White, *ACS Catal.*, **2014**, 4, 3039–3044.
[127] M. Bocus, L. Vanduyfhuys, F. De Proft, B. M. Weckhuysen, V. Van Speybroeck, *JACS Au*, **2022**, 2, 502–514.
[128] A. D. Chowdhury, A. L. Paioni, K. Houben, G. T. Whiting, M. Baldus, B. M. Weckhuysen, *Angew. Chem. Int. Ed.*, **2018**, 57, 8095–8099.
[129] P. Bollini, T. T. Chen, M. Neurock, A. Bhan, *Catal. Sci. Technol.*, **2019**, 9, 4374–4383.
[130] P. Cheung, A. Bhan, G. J. Sunley, D. J. Law, E. Iglesia, *J. Catal.*, **2007**, 245, 110–123.
[131] J. Zhou, J. Zhao, J. Zhang, T. Zhang, M. Ye, Z. Liu, *Chin. J. Catal.*, **2020**, 41, 1048–1061.
[132] J. Zhou, M. Gao, J. Zhang, W. Liu, T. Zhang, H. Li, Z. Xu, M. Ye, Z. Liu, *Nat. Commun.*, **2021**, 12, 17.
[133] J. Zhou, J. Zhang, Y. Zhi, J. Zhao, T. Zhang, M. Ye, Z. Liu, *Ind. Eng. Chem. Res.*, **2018**, 57, 17338–17347.
[134] C. Wang, L. Yang, M. Gao, X. Shao, W. Dai, G. Wu, N. Guan, Z. Xu, M. Ye, L. Li, *J. Am. Chem. Soc.*, **2022**, 144, 21408–21416.

水在分子筛催化中的相互作用：骨架结构演变与反应调控机制

何林海[a,b,l], 楼才溢[a,b,l], 孙　璐[a,b], 牛　晶[a], 徐舒涛[a,b,*], 魏迎旭[a,b], 刘中民[a,b,*]
[a]中国科学院大连化学物理研究所, 低碳催化技术国家工程研究中心, 辽宁大连116023
[b]中国科学院大学, 北京100049

摘要: 分子筛催化剂, 包括硅铝酸盐类沸石和硅铝磷酸盐类分子筛, 因具有独特的孔道结构、可调控的酸性及优异的水热稳定性, 在多相催化领域展现出广泛应用, 并有望在推动碳中和与可持续发展进程中发挥关键作用. 水分子普遍存在于分子筛材料的合成、储存及催化应用的过程中, 其与分子筛骨架之间复杂的主-客体相互作用及对骨架结构与催化性能的影

响, 近年来日益成为学术界关注的前沿科学问题. 然而, 水分子的作用机制十分复杂, 受到温度、水的相态(气态或液态)及其分压等多种因素的显著影响. 目前, 关于水与分子筛骨架之间的主-客体相互作用及水在催化过程中的作用机制仍缺乏系统性认识, 因此对相关研究进展进行全面梳理与总结具有重要意义.

本综述系统梳理了近年来围绕水与分子筛之间的相互作用及其对催化反应路径与性能调控机制影响的研究进展, 综合分析了实验表征与理论计算两方面的最新成果. 重点聚焦水环境中水分子诱导硅铝酸盐与硅铝磷酸盐类分子筛骨架在原子尺度发生的可逆与不可逆结构演变过程, 涵盖了水分子的吸附、T–O–T键的可逆水解和不可逆水解过程, 强调了分子筛骨架在水环境下所表现出的动态特性. 在催化反应层面, 文章从两个角度探讨了水分子在分子筛催化反应性能及动力学行为的双重调控机制: 一方面, 水分子可通过氢键相互作用参与反应过程, 表现为对活性位的竞争吸附、对反应基态与过渡态的稳定作用, 以及构建质子迁移桥梁等多种作用机制; 另一方面, 水分子亦可作为反应物, 直接参与反应中间体或其他客体分子的反应生成新物种. 最后, 总结了当前分子筛催化领域中水的微观作用机制解析所面临的主要挑战, 并对未来的研究方向进行了展望.

综上, 本综述旨在为深入理解含水反应过程中水分子诱导的分子筛骨架结构动态演变、阐明复杂催化反应机理, 以及优化催化反应性能提供理论参考.

关键词: 水; 分子筛; 主-客体相互作用; 分子筛催化; 水促进/抑制催化

收稿日期: 2025-06-27. 接受日期: 2025-08-10. 上网时间: 2025-12-05.

*通讯联系人. 电子信箱: xushutao@dicp.ac.cn (徐舒涛), liuzm@dicp.ac.cn (刘中民).

[1]共同第一作者.

基金来源: 国家重点研发计划(2022YFE0116000); 国家自然科学基金(22241801, 22288101, 22022202, 22032005, 21991090, 21991092, 21991093); 大连市杰出青年科技人才项目(2021RJ01); 辽宁省国际联合实验室项目(2024JH2/102100005).